AFRL-ML-WP-TR-2001-4017

COMPOSITE MATERIALS FOR ADVANCED GLOBAL MOBILITY CONCEPTS

SANGWOOK SIHN
K. KEN HAN

UNIVERSITY OF DAYTON RESEARCH INSTITUTE
300 COLLEGE PARK AVENUE
DAYTON, OH 45469-0168

OCTOBER 2000

FINAL REPORT FOR PERIOD 15 SEPTEMBER 1999 – 31 JULY 2000

REPORT DOCUMENTATION PAGE

1. REPORT DATE (DD-MM-YYYY) 01-10-2000	2. REPORT TYPE Final Report	3. DATES COVERED (FROM - TO) 15-09-1999 to 31-07-2000	
4. TITLE AND SUBTITLE Composite Materials for Advanced Global Mobility Concepts Unclassified		5a. CONTRACT NUMBER	
		5b. GRANT NUMBER	
		5c. PROGRAM ELEMENT NUMBER	
6. AUTHOR(S) Sihn, Sangwook ; Han, K. K. ;		5d. PROJECT NUMBER	
		5e. TASK NUMBER	
		5f. WORK UNIT NUMBER	
7. PERFORMING ORGANIZATION NAME AND ADDRESS University of Dayton Research Institute 300 College Park Avenue Dayton , OH 45469-0168		8. PERFORMING ORGANIZATION REPORT NUMBER	
9. SPONSORING/MONITORING AGENCY NAME AND ADDRESS Materials & Manufacturing Directorate Air Force Research Laboratory, Air Force Materiel Command Wright-Patterson AFB , OH 45433-7750		10. SPONSOR/MONITOR'S ACRONYM(S)	
		11. SPONSOR/MONITOR'S REPORT NUMBER(S)	

12. DISTRIBUTION/AVAILABILITY STATEMENT
A
PUBLIC RELEASE

Materials & Manufacturing Directorate
Air Force Research Laboratory, Air Force Materiel Command

Wright-Patterson AFB , OH 45433-7750

13. SUPPLEMENTARY NOTES

14. ABSTRACT

A 3-D stress and strain model of woven fabric composites based on Reissner's variational principle was developed and the model included 29 unknown variables. Strength predictions were also included, obtained by introducing penalty energy terms. The model results show good agreement when compared with woven composite experiments and flat laminate experiments and models. This agreement includes moduli, strength, and failure modes. Similar 3-D modeling of graphitic foam structures was initiated using the tetrahedral strut geometry. The basic premise for the graphitic foam processing model was also laid out.

15. SUBJECT TERMS

Composite modeling; mechanical modeling; process modeling, graphitic foam; 3-D model; woven fabrics; Reissner's variational principle; penalty method; mixed finite element method; free-edge problem; open-cell foam; beam; frame structure

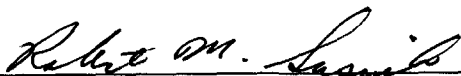| 16. SECURITY CLASSIFICATION OF:			17. LIMITATION OF ABSTRACT	18. NUMBER OF PAGES 62	19a. NAME OF RESPONSIBLE PERSON Fenster, Lynn lfenster@dtic.mil
a. REPORT Unclassified	**b. ABSTRACT** Unclassified	**c. THIS PAGE** Unclassified	Public Release		**19b. TELEPHONE NUMBER International Area Code** **Area Code Telephone Number** 703 767-9007 **DSN** 427-9007

NOTICE

Using government drawings, specifications, or other data included in this document for any purpose other than government procurement does not in any way obligate the US Government. The fact that the government formulated or supplied the drawings, specifications, or other data does not license the holder or any other person or corporation or convey any rights or permission to manufacture, use, or sell any patented invention that may relate to them.

This report is releasable to the National Technical Information Service (NTIS). At NTIS, it will be available to the general public, including foreign nations.

This technical report has been reviewed and is approved for publication.

L. SCOTT THEIBERT, Chief
Structural Materials Branch
Nonmetallic Materials Division

ROBERT M. SUSNIK, Assistant Chief
Nonmetallic Materials Division
Materials and Manufacturing Directorate

Do not return copies of this report unless contractual obligations or notice on a specific document requires its return.

REPORT DOCUMENTATION PAGE

The public reporting burden for this collection of information is estimated to average 1 hour per response, including the time for reviewing instructions, searching existing data sources, gathering and maintaining the data needed, and completing and reviewing the collection of information. Send comments regarding this burden estimate or any other aspect of this collection of information, including suggestions for reducing the burden, to Department of Defense, Washington Headquarters Services, Directorate for Information Operations and Reports (0704-0188), 1215 Jefferson Davis Highway, Suite 1204, Arlington, VA 22202-4302. Respondents should be aware that notwithstanding any other provision of law, no person shall be subject to any penalty for failing to comply with a collection of information if it does not display a currently valid OMB control number.
PLEASE DO NOT RETURN YOUR FORM TO THE ABOVE ADDRESS.

1. REPORT DATE *(DD-MM-YYYY)* OCTOBER 2000	2. REPORT TYPE FINAL REPORT	3. DATES COVERED *(From - To)* 09/15/1999-07/31/2000

4. TITLE AND SUBTITLE
COMPOSITE MATERIALS FOR ADVANCED GLOBAL MOBILITY CONCEPTS

5a. CONTRACT NUMBER
F33615-95-D-5029

5b. GRANT NUMBER

5c. PROGRAM ELEMENT NUMBER
62102F

6. AUTHOR(S)
SANGWOOK SIHN AND K. KEN HAN

5d. PROJECT NUMBER
4347

5e. TASK NUMBER
34

5f. WORK UNIT NUMBER
10

7. PERFORMING ORGANIZATION NAME(S) AND ADDRESS(ES)

UNIVERSITY OF DAYTON RESEARCH INSTITUTE
300 COLLEGE PARK AVENUE
DAYTON, OH 45469-0168

8. PERFORMING ORGANIZATION REPORT NUMBER

UDR-TR-2000-00113

9. SPONSORING/MONITORING AGENCY NAME(S) AND ADDRESS(ES)
MATERIALS AND MANUFACTURING DIRECTORATE
AIR FORCE RESEARCH LABORATORY
AIR FORCE MATERIEL COMMAND
WRIGHT-PATTERSON AFB, OH 45433-7750

10. SPONSOR/MONITOR'S ACRONYM(S)
AFRL/MLBC

11. SPONSOR/MONITOR'S REPORT NUMBER(S)
AFRL-ML-WP-TR-2001-4017

12. DISTRIBUTION/AVAILABILITY STATEMENT
APPROVED FOR PUBLIC RELEASE; DISTRIBUTION UNLIMITED.

13. SUPPLEMENTARY NOTES

14. ABSTRACT
A 3-D stress and strain model of woven fabric composites based on Reissner's variational principle was developed and the model included 29 unknown variables. Strength predictions were also included, obtained by introducing penalty energy terms. The model results show good agreement when compared with woven composite experiments and flat laminate experiments and models. This agreement includes moduli, strength, and failure modes. Similar 3-D modeling of graphitic foam structures was initiated using the tetrahedral strut geometry. The basic premise for the graphitic foam processing model was also laid out.

15. SUBJECT TERMS
Composite modeling, mechanical modeling, process modeling, graphitic foam, 3-D model, woven fabrics, Reissner's variational principle, penalty method, mixed finite element method, free-edge problem, open-cell foam, beam, frame structure

16. SECURITY CLASSIFICATION OF:			17. LIMITATION OF ABSTRACT	18. NUMBER OF PAGES	19a. NAME OF RESPONSIBLE PERSON L. SCOTT THEIBERT/AFRL/MLBC
a. REPORT U	b. ABSTRACT U	c. THIS PAGE U	SAR	62	19b. TELEPHONE NUMBER *(Include area code)* 937/255-9070

CONTENTS

FIGURES

TABLES

FOREWORD

EXECUTIVE SUMMARY

A three-dimensional model for a stress analysis of woven fabric composites, which was derived previously based on Reissner's mixed variational principle, was solved numerically with a finite element approach. Since the mixed model calculates the stress field by taking variations of displacement and stresses independently and satisfying equilibrium of stresses pointwise, accurate interlaminar stresses are predicted at the yarn interface. The interfacial continuity conditions are implemented through a penalty method by adding an additional variational energy of two constraint conditions: the displacements must be continuous along the interface between two stacked subregions, and interfacial normal and shear stresses must be in equilibrium at the interface.

After performing the thickness integration, the three-dimensional variational energy equation is evaluated for each yarn (subregion) two-dimensionally with 16 stress-related and 13 displacement-related unknown variables. Using the Rayleigh-Ritz approximation yields a system of linear equations by taking derivatives of the variational energy equation with respect to the independent unknown variables. The present mixed method is applied to the analysis of both flat and woven laminated composites. The displacement and stress results of the present method are compared and validated with the conventional displacement-based finite element solutions and/or the existing analytic solution.

The present model is also applied to the analysis of stiffness and strength of flat and woven fabric composites. The model calculates three-dimensional effective elastic moduli and predicts failure strengths and damage modes. The failure analysis includes residual stress calculation to consider the hygrothermal effect. The numerical calculations show good

1

agreement with existing experimental and numerical results on both flat and woven laminated composites with various yarn-waviness ratios.

The emerging ultra-lightweight material, carbon foam, was modeled with the three-dimensional microstructures to develop a basic understanding of the performance of open-cell foam materials. The model can describe the deformation behavior accurately and will be used to investigate the failure mechanism of the cell ligaments.

Because of the randomness and complexity of the microstructure of the carbon foam, the representative cell ligaments are first characterized in detail at the microstructural level. The microstructural characterization will then be correlated with the macroscopic bulk properties by a statistical approach. A series of databases will be collected for various size and spatial orientation of the cell ligaments, as well as the property variation due to the graphic alignment along the longitudinal direction of the ligaments.

Because of slenderness, each ligament can be considered as a beam, and the tetrahedral cell microstructure with four ligaments as a frame structure. The four beams are located in three-dimensional space under arbitrary loading conditions. The cross section of the beam varies in size and material properties in the longitudinal direction along the ligament.

Based on the literature review, the research approach of modeling the carbon foam blowing process was developed. The model consists of three concepts: (1) nucleation of microcellular that determines the relationship of the cell number, gas kind, temperature and pressure, (2) bubble growth that calculates bubble dynamic size and shape so the relationship of the process parameters and foam properties can be determined, and (3) mold filling that simulates the process of the foam filling a mold cavity. A finite element code is being developed.

1. THREE-DIMENSIONAL MODELING OF WOVEN COMPOSITES

1.1 INTRODUCTION

To achieve the optimum structural properties of state-of-the-art fabric reinforcements of woven composites, there is a need to develop a basic understanding of deformation and damage mechanisms. A model for three-dimensional stress analysis of woven fabric composites has been proposed by Roy [1] to obtain reliable three-dimensional stress fields, especially interlaminar stresses along interfaces between yarns. The model is formulated based on Reissner's mixed variational principle to take independent variations on the stress and the displacement components [2-4]. The in-plane stresses within a yarn are assumed to vary linearly in the thickness direction, and the expressions for the interlaminar stresses are obtained by satisfying the three-dimensional equilibrium equations. After performing the thickness integration, the three-dimensional variational energy equation becomes a two-dimensional equation. The variational equation is expressed with 16 stress-related and 13 displacement-related unknown variables. In this model, an accurate calculation of the interlaminar stresses at the yarn (subregion) interface can be achieved (except near the point of singularity) by satisfying the interfacial traction continuity conditions and the equilibrium of stresses pointwise.

Our present work establishes a mixed finite element analysis (FEA) based on the mixed variational principle. Total variational energy is obtained by accumulating the energy for all yarn and matrix subregions. The subregions are further discretized into finite elements in a plane perpendicular to the thickness direction. The interfacial continuity conditions are implemented through a penalty method by adding an additional variational energy of two constraint conditions: the displacements must be continuous along the interface between two stacked subregions, and interfacial normal and shear stresses must be in equilibrium at the interface.

Two large numbers of penalty parameters enforcing the displacement and stress continuity are employed carefully to avoid numerical errors. The solution of the variational energy equation is obtained by using the Rayleigh-Ritz approximation with polynomial shape functions.

The present mixed method is applied to analyze a flat laminated composite with a free edge and a representative volume element (RVE) of plain-weave composites. The displacement and stress results of the present method are compared with the conventional displacement-based finite element solutions and/or the existing analytic solutions. The reliable prediction of the stress field by the present method is used to calculate stiffness and strength of the flat/woven laminated composites. Three-dimensional effective elastic moduli are calculated for several flat/woven laminated composites and compared with existing experimental/numerical results. Meanwhile, a discrete damage analysis is achieved to calculate first-ply and last-ply failure loads as well as their damage modes. Failure strengths are predicted by considering not only mechanical stresses but also residual stresses that are significantly influenced by hygrothermal effects. The numerical predictions on the failure strength and the damage mode are compared with experimental results that were previously observed on flat laminated composites and woven model laminates with one-dimensional yarn crimping.

1.2 FORMULATION OF THREE-DIMENSIONAL MODEL

1.2.1 Modified Variational Energy Equation

The variational energy equation evaluated for a given (k-th) subregion is written as

$$
\begin{aligned}
J^{(k)} = &\iint_{xy} \left[(\boldsymbol{m}_{ij} + \boldsymbol{c}_{ij}) p_{ij} - (F_1 \bar{u} + F_2 u^* + F_3 \bar{v} + F_4 v^* + F_5 \bar{w} + F_6 w^* + F_7 \hat{w}) \right]^{(k)} dx\, dy \\
&+ \iint_{xy} \left[\left(p_{52} - h_{2,x} p_{12} - h_{2,y} p_{62} \right) u_2 - \left(p_{51} - h_{1,x} p_{11} - h_{1,y} p_{61} \right) u_1 \right.
\end{aligned}
\tag{1}
$$

4

$$+ \left(p_{42} - h_{2,x} p_{62} - h_{2,y} p_{22} \right) v_2 - \left(p_{41} - h_{1,x} p_{61} - h_{1,y} p_{21} \right) v_1$$

$$+ \left. \left(p_{32} - h_{2,x} p_{52} - h_{2,y} p_{42} \right) w_2 - \left(p_{31} - h_{1,x} p_{51} - h_{1,y} p_{41} \right) w_1 \right]^{(k)} dxdy$$

$$+ \int_x \left[\left(p_{61} \overline{u} + p_{62} u^* + p_{21} \overline{v} + p_{22} v^* + p_{41} \overline{w} + p_{42} w^* + p_{43} \hat{w} \right) \left(h_2 - h_1 \right) \right]^{(k)} \Big|_{y_1}^{y_2} dx$$

$$+ \int_y \left[\left(p_{11} \overline{u} + p_{12} u^* + p_{61} \overline{v} + p_{62}^{(k)} v^* + p_{51} \overline{w} + p_{52} w^* + p_{53} \hat{w} \right) \left(h_2 - h_1 \right) \right]^{(k)} \Big|_{x_1}^{x_2} dy$$

$$- \int_{\tilde{A}} \left[\left(\boldsymbol{\tau}_{x2} u_2 + \boldsymbol{\tau}_{y2} v_2 + \boldsymbol{\tau}_{z2} w_2 \right) - \left(\boldsymbol{\tau}_{x1} u_1 + \boldsymbol{\tau}_{y1} v_1 + \boldsymbol{\tau}_{z1} w_1 \right) \right]^{(k)} d\tilde{A} \quad = \quad 0$$

where $\boldsymbol{m}_{ij}$ and $\boldsymbol{c}_{ij}$ are defined in Roy [1].

The interfacial continuity condition dictates that the displacements must be continuous along the interface between two stacked subregions (k-th and l-th subregions), and interfacial normal and shear stresses must be in equilibrium, as Figure 1 shows.
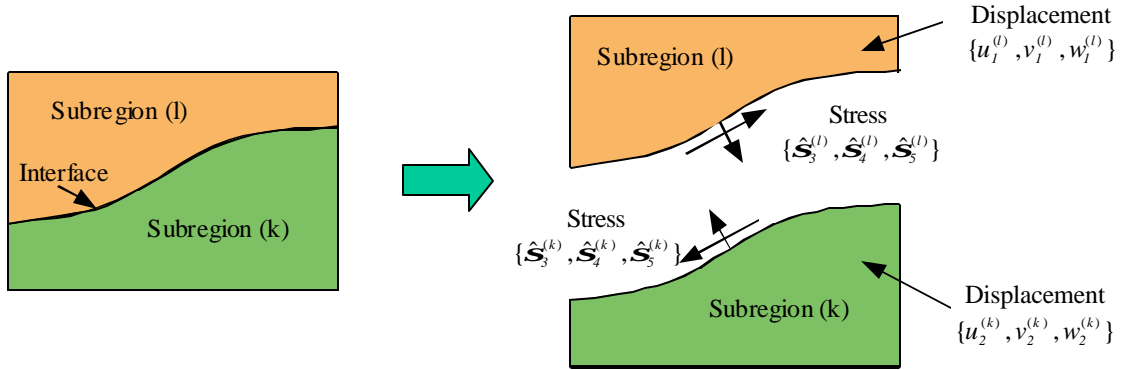
Figure 1. Displacement and Stress Continuity at the Interface between k-th and l-th Subregions.

By setting the interfacial normal stress as $\hat{s}_3$ and interfacial shear stresses as $\hat{s}_4$ and $\hat{s}_5$, the interfacial continuity condition provides the following constraint conditions:

(1) Displacement continuity:

$$u_2^{(k)} - u_1^{(l)} = 0$$

$$v_2^{(k)} - v_1^{(l)} = 0 \qquad (2)$$

$$w_2^{(k)} - w_1^{(l)} = 0$$

5

(2) Normal and shear stress continuity:

$$\hat{\boldsymbol{s}}_3^{(k)} - \hat{\boldsymbol{s}}_3^{(l)} = 0$$

$$\hat{\boldsymbol{s}}_4^{(k)} - \hat{\boldsymbol{s}}_4^{(l)} = 0 \tag{3}$$

$$\hat{\boldsymbol{s}}_5^{(k)} - \hat{\boldsymbol{s}}_5^{(l)} = 0$$

where $\hat{\boldsymbol{s}}_i^{(k)}$ and $\hat{\boldsymbol{s}}_i^{(l)}$ are the interfacial stress components at the k-th and l-th subregions, respectively. Note that the interfacial stresses are evaluated in a local coordinate system whose planar coordinates are parallel to the interfacial surfaces. These local stress components along the interfacial surfaces are related with stress components in the global coordinates by the slopes of the interfacial surfaces in x- and y-directions ($h_{2,x}^{(k)}$ and $h_{2,y}^{(k)}$). Stress transformation using the direction cosines of the interfacial surface vectors yields the following stress constraint equations in the global coordinate system:

$$\hat{\boldsymbol{s}}_3^{(k)} - \hat{\boldsymbol{s}}_3^{(l)} = 0 \implies \boldsymbol{s}_3^{(k)} - \boldsymbol{s}_3^{(l)} - h_{2,x}^{(k)} \cdot (\boldsymbol{s}_5^{(k)} - \boldsymbol{s}_5^{(l)}) - h_{2,y}^{(k)} \cdot (\boldsymbol{s}_4^{(k)} - \boldsymbol{s}_4^{(l)}) = 0$$

$$\hat{\boldsymbol{s}}_4^{(k)} - \hat{\boldsymbol{s}}_4^{(l)} = 0 \implies \boldsymbol{s}_4^{(k)} - \boldsymbol{s}_4^{(l)} - h_{2,x}^{(k)} \cdot (\boldsymbol{s}_6^{(k)} - \boldsymbol{s}_6^{(l)}) - h_{2,y}^{(k)} \cdot (\boldsymbol{s}_2^{(k)} - \boldsymbol{s}_2^{(l)}) = 0 \tag{4}$$

$$\hat{\boldsymbol{s}}_5^{(k)} - \hat{\boldsymbol{s}}_5^{(l)} = 0 \implies \boldsymbol{s}_5^{(k)} - \boldsymbol{s}_5^{(l)} - h_{2,x}^{(k)} \cdot (\boldsymbol{s}_1^{(k)} - \boldsymbol{s}_1^{(l)}) - h_{2,y}^{(k)} \cdot (\boldsymbol{s}_6^{(k)} - \boldsymbol{s}_6^{(l)}) = 0$$

To impose the constraint conditions for displacement and stress continuity, one can substitute them into equation (1) directly to formulate an irreducible form. It is straightforward to substitute the displacement continuity. However, it turns out that substituting the stress continuity requires an extremely involved algebraic manipulation. Moreover, when obtaining numerical solutions by using polynomial shape functions, the restriction of excessive continuity for stresses should be avoided at singularities and/or at abrupt changes in material properties. The imposition of such continuity would likely produce erroneous and usually highly oscillating results [5].

Instead of using the irreducible form, a penalty approach is employed by adding a new energy term (J_c) for the constraint conditions, with penalty parameters ($\mathbf{a}_1$ and $\mathbf{a}_2$), which yields the following modified variational energy equation:

$$\bar{J} = \sum_{k=1}^{M} J^{(k)} + \sum_{k=1}^{M-1} J_c^{(k)} \tag{5}$$

where

$$J_c^{(k)} = \frac{1}{2} \cdot \mathbf{a}_1 \cdot \iint_{xy} \left[(u_2^{(k)} - u_1^{(l)})^2 + (v_2^{(k)} - v_1^{(l)})^2 + (w_2^{(k)} - w_1^{(l)})^2 \right] dxdy$$

$$+ \frac{1}{2} \cdot \mathbf{a}_2 \cdot \iint_{xy} \left[(\hat{\mathbf{s}}_3^{(k)} - \hat{\mathbf{s}}_3^{(l)})^2 + (\hat{\mathbf{s}}_4^{(k)} - \hat{\mathbf{s}}_4^{(l)})^2 + (\hat{\mathbf{s}}_5^{(k)} - \hat{\mathbf{s}}_5^{(l)})^2 \right] dxdy \tag{6}$$

and M is the number of subregions in the thickness (z) direction. Two large numbers of $\mathbf{a}_1$ and $\mathbf{a}_2$ enforce the displacement and stress continuity, respectively. However, $\mathbf{a}_2$ must be selected carefully to avoid the excessive continuity for stresses. Because of the nature of the mixed formulation for the stress and the displacements, erroneous results in stress may ruin the ones in displacement, and vice versa. The effect of the penalty parameters will be discussed later.

Because of the complexity of the modified variational equation, it is more desirable to obtain the solution numerically rather than analytically. Using the Rayleigh-Ritz approximation can yield a system of linear equations that is solvable numerically. There are two possible approaches, finite element or finite difference, which can be taken to solve the system of equations numerically, and the former is taken in this study.

Because of the through-the-thickness (z) integration during formulation, the modified mixed variational equation, equation (5), is only a function of x and y, and so are the 29*Ns unknown variables ($C_i^{(k)}(x, y)$, $i = 1, \cdots, 29$) for the k-th subregion, where Ns is the

number of subregions. Among 29 unknown variables for each subregion, 16 are for the stress components, and 13 are for the displacement components, as in equation (8). The variational equation is then discretized in x- and y-directions for the finite element formulation. The unknown variables are collected in a vector, as follows:

$$\left\{C_i^{(k)}(x, y)\right\} = \left\{ \begin{array}{c} \mathbf{p}^{(k)} \\ \mathbf{d}^{(k)} \end{array} \right\} \tag{7}$$

where

$$\mathbf{p}^{(k)} = \left\{ p_{11}, p_{12}, p_{21}, p_{22}, p_{31}, p_{32}, p_{33}, p_{34}, p_{41}, p_{42}, p_{43}, p_{51}, p_{52}, p_{53}, p_{61}, p_{62} \right\}^{(k)T}$$

and

$$\mathbf{d}^{(k)} = \left\{ \overline{u}, u^*, u_1, u_2, \overline{v}, v^*, v_1, v_2, \overline{w}, w^*, \hat{w}, w_1, w_2 \right\}^{(k)T}$$

(8)

Each of the unknown variables, $C_i^{(k)}(x, y)$, are then interpolated with their nodal contribution, $C_{ij}^{(k)}$, by shape functions, as follows:

$$p_i^{(k)}(x, y) = \sum_{j=1}^{Nen} p_{ij}^{(k)} \cdot N_{pj}(x, y)$$

$$d_i^{(k)}(x, y) = \sum_{j=1}^{Nen} d_{ij}^{(k)} \cdot N_{dj}(x, y)$$

(9)

where N_{en} is the number of nodal points in an element, and N_{pj} and N_{dj} are the shape functions for the stress and displacement degrees of freedom, respectively. The shape functions can be chosen as the linear polynomial for 4-node quadrilateral elements ($N_{en} = 4$), quadratic polynomial for 8-node serendipity elements ($N_{en} = 8$), etc.

The nodal values of the unknown variables for each finite element are collected in a vector, as follows:

8

$$\mathbf{C}^{(k)}(x,y) = \left\{C_{ij}^{(k)}\right\} = \left\{\mathbf{p}_1, \mathbf{d}_1, \mathbf{p}_2, \mathbf{d}_2, \cdots, \mathbf{p}_j, \mathbf{d}_j, \cdots, \mathbf{p}_{Nen}, \mathbf{d}_{Nen}\right\}^{(k)T} \tag{10}$$

where

$$\mathbf{p}_j = \left\{p_{11}, p_{12}, p_{21}, p_{22}, p_{31}, p_{32}, p_{33}, p_{34}, p_{41}, p_{42}, p_{43}, p_{51}, p_{52}, p_{53}, p_{61}, p_{62}\right\}_j^T$$

and

$$\tag{11}$$

$$\mathbf{d}_j = \left\{\overline{u}, u^*, u_1, u_2, \overline{v}, v^*, v_1, v_2, \overline{w}, w^*, \hat{w}, w_1, w_2\right\}_j^T$$

The Rayleigh-Ritz approximation yields a system of linear equations by taking derivatives of the variational energy equation with respect to the independent unknown variables, as follows:

$$\frac{\partial J^{(k)}}{\partial C_{ij}^{(k)}} = 0 \tag{12}$$

The system of equations is then expressed in the matrix form, as follows:

$$\begin{bmatrix} \mathbf{A} & \mathbf{C} \\ \mathbf{C}^T & \mathbf{0} \end{bmatrix}^{(k)} \begin{Bmatrix} \mathbf{p} \\ \mathbf{d} \end{Bmatrix}^{(k)} = \begin{Bmatrix} \mathbf{f}_1 \\ \mathbf{f}_2 \end{Bmatrix}^{(k)} \tag{13}$$

with

$$\mathbf{A} = \int_{\grave{U}} \mathbf{N}_\mathbf{p}^T \, \mathbf{S} \, \mathbf{N}_\mathbf{p} \, d\grave{U}$$

$$\mathbf{C} = \int_{\grave{U}} \mathbf{N}_\mathbf{p}^T \, \mathbf{B} \, \mathbf{N}_\mathbf{d} \, d\grave{U}$$

$$\tag{14}$$

$$\mathbf{f}_1 = \mathbf{0}$$

$$\mathbf{f}_2 = \int_{\tilde{A}_\acute{o}} \mathbf{N}_\mathbf{d}^T \, \tilde{\mathbf{o}} \, d\tilde{A}$$

where $\mathbf{S}, \mathbf{B}, \mathbf{N}_\mathbf{p}$ and $\mathbf{N}_\mathbf{d}$ are matrices for the compliance, relationship between the stresses and displacements, and the shape functions for the stress and displacement degree of freedoms, respectively.

The equations for the constraint conditions at the interface are also obtained by

$$\frac{\partial J_c^{(k)}}{\partial C_{ij}^{(k)}} = 0 \quad \text{and} \quad \frac{\partial J_c^{(k)}}{\partial C_{ij}^{(l)}} = 0 \tag{15}$$

which yields another matrix form, as follows:

$$\begin{bmatrix} \mathbf{Q_P} & \mathbf{0} & -\mathbf{Q_P} & \mathbf{0} \\ \mathbf{0} & \mathbf{Q_d} & \mathbf{0} & -\mathbf{Q_d} \\ -\mathbf{Q_P^T} & \mathbf{0} & \mathbf{Q_P} & \mathbf{0} \\ \mathbf{0} & -\mathbf{Q_d^T} & \mathbf{0} & \mathbf{Q_d} \end{bmatrix} \begin{Bmatrix} \mathbf{p}^{(k)} \\ \mathbf{d}^{(k)} \\ \mathbf{p}^{(l)} \\ \mathbf{d}^{(l)} \end{Bmatrix} = \mathbf{0} \tag{16}$$

with

$$\mathbf{Q_d} = \mathbf{a}_1 \int_{\grave{U}} \mathbf{N_d^T} \, \mathbf{N_d} \, d\grave{U}$$

$$\mathbf{Q_P} = \mathbf{a}_2 \int_{\grave{U}} \mathbf{N_p^T} \, \mathbf{h_{,x}} \, \mathbf{N_p} \, d\grave{U} \tag{17}$$

where $\mathbf{h_{,x}}$ is a matrix containing the slopes of the interfacial surfaces in x- and y-directions as in equation (4). The global system of equations is then formulated by combining the elemental stiffness matrix and force vectors in equation (13) and equation (16), and solved numerically to obtain the displacement and stress results.

1.2.2 Calculation of Effective Elastic Moduli

Effective elastic moduli of the woven composites are calculated by solving six different cases under uniform axial and shear strain loadings ($\bar{e}_i$). The boundary conditions for each loading case are as follows:

(1) For $\bar{e}_1 = \bar{\mathbf{e}}_x = U_o / L_x$,

$$u(0, y, z) = 0 \quad , \quad u(L_x, y, z) = U_o$$

$$v(x, 0, z) = v(x, L_y, z) = 0 \tag{18}$$

$$w(x, y, 0) = w(x, y, L_z) = 0$$

(2) For $\bar{e}_2 = \bar{e}_y = V_o/L_y$,

$$u(0, y, z) = u(L_x, y, z) = 0$$

$$v(x, 0, z) = 0 \quad , \quad v(x, L_y, z) = V_o \quad\quad (19)$$

$$w(x, y, 0) = w(x, y, L_z) = 0$$

(3) For $\bar{e}_3 = \bar{e}_z = W_o/L_z$,

$$u(0, y, z) = u(L_x, y, z) = 0$$

$$v(x, 0, z) = v(x, L_y, z) = 0 \quad\quad (20)$$

$$w(x, y, 0) = 0 \quad , \quad w(x, y, L_z) = W_o$$

(4) For $\bar{e}_4 = \bar{g}_{yz} = V_o/L_z$,

$$u(0, y, z) = u(L_x, y, z) = 0$$

$$v(x, y, 0) = 0 \quad , \quad v(x, y, L_z) = V_o \quad\quad (21)$$

$$w(x, y, 0) = w(x, y, L_z) = 0$$

(5) For $\bar{e}_5 = \bar{g}_{xz} = U_o/L_z$,

$$u(x, y, 0) = 0 \quad , \quad u(x, y, L_z) = U_o$$

$$v(x, 0, z) = v(x, L_y, z) = 0 \quad\quad (22)$$

$$w(x, y, 0) = w(x, y, L_z) = 0$$

(6) For $\bar{e}_6 = \bar{g}_{xy} = U_o/L_y$,

$$u(x, 0, z) = 0 \quad , \quad u(0, L_y, z) = U_o$$

$$v(x, 0, z) = v(x, L_y, z) = 0 \quad\quad (23)$$

$$w(x, y, 0) = w(x, y, L_z) = 0$$

where U_o, V_o, W_o are the uniformly applied displacement components.

For each uniform-strain boundary condition, effective stresses ($\bar{s}_i$) are calculated by taking a volumetric average, as follows:

$$\bar{s}_i = \frac{\int_V s_i(x, y, z)\, dxdydz}{V} \quad , \quad (i = 1, \cdots, 6) \quad\quad (24)$$

11

Components of 6×6 effective stiffness matrix ($[\overline{C}_{ij}]$) and effective compliance matrix ($[\overline{S}_{ij}]$) are then obtained by the following equation:

$$\{\overline{\mathbf{s}}_i\} = [\overline{C}_{ij}]\{\overline{e}_i\} \quad \text{and} \quad [\overline{S}_{ij}] = [\overline{C}_{ij}]^{-1} \tag{25}$$

where

$$[\overline{C}_{ij}] = \begin{bmatrix} \overline{C}_{11} & \overline{C}_{12} & \overline{C}_{13} & \overline{C}_{14} & \overline{C}_{15} & \overline{C}_{16} \\ \overline{C}_{21} & \overline{C}_{22} & \overline{C}_{23} & \overline{C}_{24} & \overline{C}_{25} & \overline{C}_{26} \\ \overline{C}_{31} & \overline{C}_{32} & \overline{C}_{33} & \overline{C}_{34} & \overline{C}_{35} & \overline{C}_{36} \\ \overline{C}_{41} & \overline{C}_{42} & \overline{C}_{43} & \overline{C}_{44} & \overline{C}_{45} & \overline{C}_{46} \\ \overline{C}_{51} & \overline{C}_{52} & \overline{C}_{53} & \overline{C}_{54} & \overline{C}_{55} & \overline{C}_{56} \\ \overline{C}_{61} & \overline{C}_{62} & \overline{C}_{63} & \overline{C}_{64} & \overline{C}_{65} & \overline{C}_{66} \end{bmatrix} \tag{26}$$

Finally, the three-dimensional effective elastic moduli are calculated by the following:

$$\overline{E}_x = \frac{1}{\overline{S}_{11}}, \quad \overline{E}_y = \frac{1}{\overline{S}_{22}}, \quad \overline{E}_z = \frac{1}{\overline{S}_{33}}$$

$$\overline{G}_{yz} = \frac{1}{\overline{S}_{44}}, \quad \overline{G}_{xz} = \frac{1}{\overline{S}_{55}}, \quad \overline{G}_{xy} = \frac{1}{\overline{S}_{66}} \tag{27}$$

$$\overline{\mathbf{n}}_{xy} = -\frac{\overline{S}_{12}}{\overline{S}_{11}}, \quad \overline{\mathbf{n}}_{xz} = -\frac{\overline{S}_{13}}{\overline{S}_{11}}, \quad \overline{\mathbf{n}}_{yz} = -\frac{\overline{S}_{23}}{\overline{S}_{22}}$$

1.2.3 Calculation of Residual Stresses

When the laminated composites are cured and cooled to room temperature, residual stresses will exist because thermal contraction of each ply is anisotropic. When moisture is subsequently absorbed, hygro expansion is also anisotropic. Therefore, stress calculation in laminated composites should include both the mechanical and the residual stresses due to the hygrothermal effect. The variational energy term for the hygrothermal effect [1] is calculated as follows:

$$E_{ij}^{(k)} = \int_{h_1}^{h_2} e_i^{(k)} f_j^{(i)} dz \tag{28}$$

where $e_i^{(k)} = \{e\}_{global}^H$ are hygrothermal strain components in the global coordinate system. The

hygrothermal strain components ($\overline{e}_i^{(k)} = \{e\}_{on}^H$) in the on-axis coordinate system are expressed as

$$\overline{e}_i^{(k)} = \boldsymbol{a}_i \Delta T + \boldsymbol{b}_i c \tag{29}$$

which are related with the global ones by the following equation:

$$\{e\}_{global}^H = [T_2(\boldsymbol{q}_2)]^{-T} [T_1(\boldsymbol{q}_1)]^{-T} \{e\}_{on}^H \tag{30}$$

where ΔT is a temperature difference between curing and operating conditions, and c is

moisture content after the curing. The $\boldsymbol{q}_1$ is the angle between the principal material direction

and the yarn direction, and $\boldsymbol{q}_2$ is the angle between the yarn direction and the global coordinate

direction. The $[T_1(\boldsymbol{q}_1)]$ and $[T_2(\boldsymbol{q}_2)]$ are tensor transformation matrices for fiber orientation and

yarn-crimping angles, respectively, as follows:

$$[T_1(\boldsymbol{q}_1)] = \begin{bmatrix} m_1^2 & n_1^2 & 0 & 0 & 0 & -2m_1 n_1 \\ n_1^2 & m_1^2 & 0 & 0 & 0 & 2m_1 n_1 \\ 0 & 0 & 1 & 0 & 0 & 0 \\ 0 & 0 & 0 & m_1 & n_1 & 0 \\ 0 & 0 & 0 & -n_1 & m_1 & 0 \\ m_1 n_1 & -m_1 n_1 & 0 & 0 & 0 & m_1^2 - n_1^2 \end{bmatrix} \tag{31}$$

and for warp yarns, the following applies:

$$[T_2(\boldsymbol{q}_2)]^{warp} = \begin{bmatrix} m_2^2 & 0 & n_2^2 & 0 & 2m_2 n_2 & 0 \\ 0 & 1 & 0 & 0 & 0 & 0 \\ n_2^2 & 0 & m_2^2 & 0 & -2m_2 n_2 & 0 \\ 0 & 0 & 0 & m_2 & 0 & -n_2 \\ -m_2 n_2 & 0 & m_2 n_2 & 0 & m_2^2 - n_2^2 & 0 \\ 0 & 0 & 0 & n_2 & 0 & m_2 \end{bmatrix} \tag{32}$$

or for fill yarns, the following applies:

$$[T_2(\mathbf{q}_2)]^{fill} = \begin{bmatrix} 1 & 0 & 0 & 0 & 0 & 0 \\ 0 & m_2^2 & n_2^2 & -2m_2n_2 & 0 & 0 \\ 0 & n_2^2 & m_2^2 & 2m_2n_2 & 0 & 0 \\ 0 & m_2n_2 & -m_2n_2 & m_2^2-n_2^2 & 0 & 0 \\ 0 & 0 & 0 & 0 & m_2 & n_2 \\ 0 & 0 & 0 & 0 & -n_2 & m_2 \end{bmatrix}$$

(33)

where $m_1 = \cos(\mathbf{q}_1)$, $n_1 = \sin(\mathbf{q}_1)$, $m_2 = \cos(\mathbf{q}_2)$ and $n_2 = \sin(\mathbf{q}_2)$.

1.2.4   Calculation of Failure Strength

Failure analysis to predict the critical load and the damage mode is achieved by applying failure criteria to the reliably calculated stress components, not by interpolating the displacement results as in the displacement-based method. Assuming that all stress components increase proportionally to the applied loading, the following results:

$$\mathbf{s}_i^{max} = R\mathbf{s}_i^{applied}$$

(34)

The strength ratio (R) can be split into mechanical (R^m) and residual (R^r) parts on an assumption that each part of the stresses acts independently, so that equation (34) becomes

$$\mathbf{s}_i^{max} = R^m\mathbf{s}_i^m + R^r\mathbf{s}_i^r$$

(35)

For a given hygrothermal combination of the cure temperature and the moisture content, the residual stresses are fixed. When mechanical loads are applied to the laminate, the maximum load that the laminate can sustain is then given by the mechanical part of the strength ratio. The mechanical strength ratio can be solved by letting the residual strength ratio equal unity.

1.2.4.1 Quadratic failure criteria

Quadratic failure criteria in stress space consist of linear and quadratic invariants as follows:

$$F_{ij} \boldsymbol{s}_i^{max} \boldsymbol{s}_j^{max} + F_i \boldsymbol{s}_i^{max} - 1 = 0 \tag{36}$$

where F_{ij} and F_i are strength parameters in stress space. By letting the residual strength ratio equal unity, the following equation results:

$$a^m (R^m)^2 + (b^m + a^{mix}) R^m + (a^r + b^r - 1) = 0 \tag{37}$$

where

$$a^m = F_{ij} \boldsymbol{s}_i^m \boldsymbol{s}_j^m \quad , \quad b^m = F_i \boldsymbol{s}_i^m$$

$$a^{mix} = 2 F_{ij} \boldsymbol{s}_i^m \boldsymbol{s}_j^r \tag{38}$$

$$a^r = F_{ij} \boldsymbol{s}_i^r \boldsymbol{s}_j^r \quad , \quad b^r = F_i \boldsymbol{s}_i^r$$

In this study, the Tsai-Wu failure criterion is used with interaction terms of $F_{12}^* = F_{13}^* = -0.5$ [6].

1.2.4.2 Maximum stress failure criteria

To understand the basic damage mechanism during the load increase, it is important to identify the most critical stress component. To distinguish the most critical stress component from the others, it is advantageous to use maximum stress failure criteria. Note that there is no interaction term between the stress components. By considering both the mechanical and the residual stresses, the failure occurs when one of the following conditions is met:

(1)   For tensile or compressive stresses ($i = 1, 2, 3$):

$$\text{if } \boldsymbol{s}_i^m + \boldsymbol{s}_i^r \geq 0 \, , \; R_i^m = \frac{X_i^T - \boldsymbol{s}_i^r}{\boldsymbol{s}_i^m}$$

$$\text{if } \boldsymbol{s}_i^m + \boldsymbol{s}_i^r < 0 \, , \; R_i^m = \frac{-X_i^C - \boldsymbol{s}_i^r}{\boldsymbol{s}_i^m} \tag{39}$$

15

(2)   For shear stresses ($i = 4, 5, 6$):

$$R_i^m = \left| \frac{S_i - \mathbf{S}_i^r}{\mathbf{S}_i^m} \right| \tag{40}$$

where X_i^T, X_i^C and S_i are tensile, compressive and shear strengths, respectively.

1.3   NUMERICAL RESULTS AND DISCUSSION

The mixed finite element method is implemented into an in-house computer program, "3Dwoven." The program is based on a spreadsheet with user-friendly input and output routines.

The present method is applied to the analysis of flat and woven laminated composites. First, displacements and stresses of these composites are calculated and compared with analytic and/or conventional displacement-based finite element solutions. Second, three-dimensional effective elastic moduli are calculated for several flat/woven laminated composites, and compared with existing experimental/numerical results. Last, first-ply and last-ply failure loads as well as their damage modes are predicted with the present method. The numerical predictions on the failure strength and the damage mode are compared with experimental results that were previously observed on flat laminated composites and woven model laminates with one-dimensional yarn crimping.

1.3.1   Flat Laminated Composites

We solved a class of boundary value problems, known as the free-edge problem, in which a flat laminate of finite width is subject to a uniform axial displacement (U_o). The origin of coordinates is located at the center of the laminate, and the laminate is symmetric ($\mathbf{q}(z) = \mathbf{q}(-z)$). Each layer is treated as a transversely isotropic material with a lay-up of $[0/90]_s$,

where $0°$ is parallel with the x-axis, as in Figure 2. The layers are of equal thickness, h, and the laminate width is $2b = 16h$. The material properties are listed in Table 1.
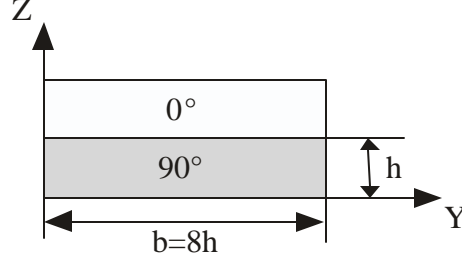

Figure 2. Flat Laminated Composites.

Table 1
Three-Dimensional Properties of Unidirectional T300/N5208 Composite

| E_x [GPa]	E_y [GPa]	E_z [GPa]	$\boldsymbol{n}_{xy}$	$\boldsymbol{n}_{xz}$	$\boldsymbol{n}_{yz}$	G_{xy} [GPa]	G_{xz} [GPa]	G_{yz} [GPa]
181	10.3	10.3	0.28	0.28	0.5	7.17	7.17	7.05

The following boundary conditions are applied to simulate a tensile loading subject to a uniform displacement in the x-direction. The axial displacement in the x-direction at $x=0$ (yz-surface) is fixed, and at $x=L_x$ is prescribed with U_o. The symmetric boundary condition is enforced at $y=0$ (xz-surface) by setting $v=0$. The zero vertical displacement at $z=0$ simulates a case in which laminates are symmetrically stacked.

$$u_1^{(k)}(0, y, z) = u_2^{(k)}(0, y, z) = 0 \quad , \quad \overline{u}^{(k)}(0, y, z) = u *^{(k)}(0, y, z) = 0$$

$$u_1^{(k)}(L_x, y, z) = u_2^{(k)}(L_x, y, z) = U_o \quad , \quad \overline{u}^{(k)}(L_x, y, z) = u *^{(k)}(L_x, y, z) = \frac{U_o}{2} \quad (41)$$

$$v_1^{(k)}(x, 0, z) = v_2^{(k)}(x, 0, z) = 0 \quad , \quad \overline{v}^{(k)}(x, 0, z) = v *^{(k)}(x, 0, z) = 0$$

$$w_1^{(k)}(x, y, 0) = 0$$

The penalty parameters in equation (6) are chosen as $a_1 = 10^3$ and $a_2 = 10^2$ to avoid numerical instability. Two different meshes are generated for the present mixed method: having the same number of divisions in the y-axis, one has only one sublayer, and the other has three sublayers in each ply (subregion) in the z-axis. The number of divisions and mesh are shown in Figure 3 (a) and (b).

Stress and displacement results are compared with the analytic and the displacement-based finite element solutions. The analytic solutions are obtained by a two-dimensional mixed analysis with 18 sublayers suggested by Pagano [3]. For the displacement-based finite element method, three-dimensional eight-node brick elements are used with two different meshes; one has two divisions and the other has 10 divisions in the z-direction in each subregion, as in Figure 3 (c) and (d). The interfacial stresses are calculated by interpolating the elemental stresses at the Gaussian integration points into the nodal points along the interface. Thus, two normal and shear stresses are calculated by interpolating those of the upper and the lower elements at the interface.

Figure 4 shows the results of the present method (mixed) compared with the analytic and FEM solutions. The results show that the normal and shear stresses become singular at the free-edge ($y = L_y$) because of the discontinuity in the elastic properties. The present and analytic methods, which are both the mixed methods, yield nearly identical results for the transverse displacement at the top surface [Figure 4 (a)], the normal stress along the [0/90] interface [Figure 4 (b)], and the normal stress along the central surface [Figure 4 (d)], whereas the displacement-based FEM shows little difference with them. The FEM does not yield an accurate solution without a sufficient number of sublayers in the z-direction, whereas the present method shows an excellent agreement even with one layer except at a region close to the free edge.
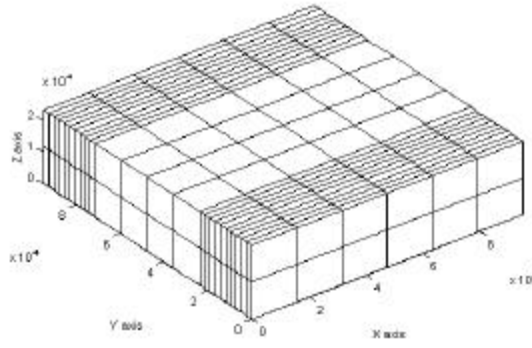
(a) Mixed ($N_x = 6$, $N_y = 24$, $N_z = 1$).
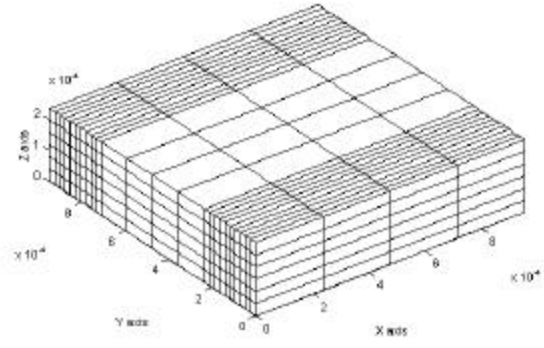
(b) Mixed ($N_x = 4$, $N_y = 24$, $N_z = 3$).
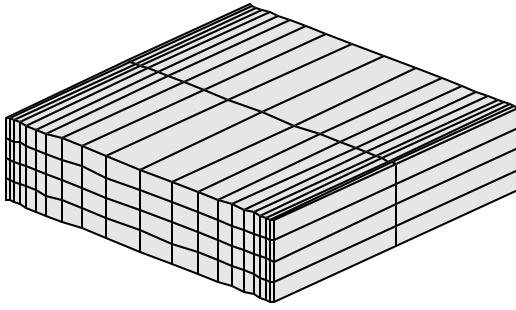
(c) FEM ($N_x = 2$, $N_y = 20$, $N_z = 2$).
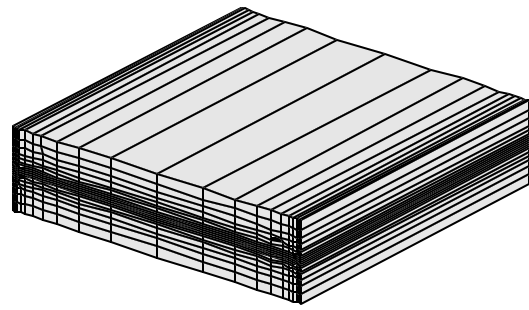
(d) FEM ($N_x = 1$, $N_y = 20$, $N_z = 10$).

Figure 3.   Geometry and Number of Divisions for Present Mixed and Displacement-Based Finite Element Methods.

19
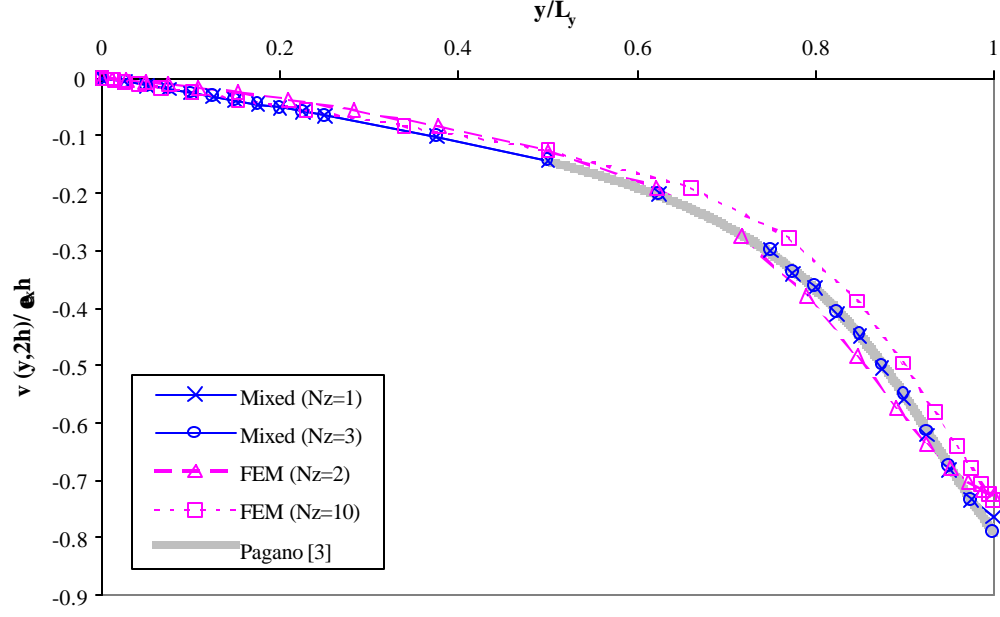
(a) Transverse displacement at top surface ($z = 2h$)
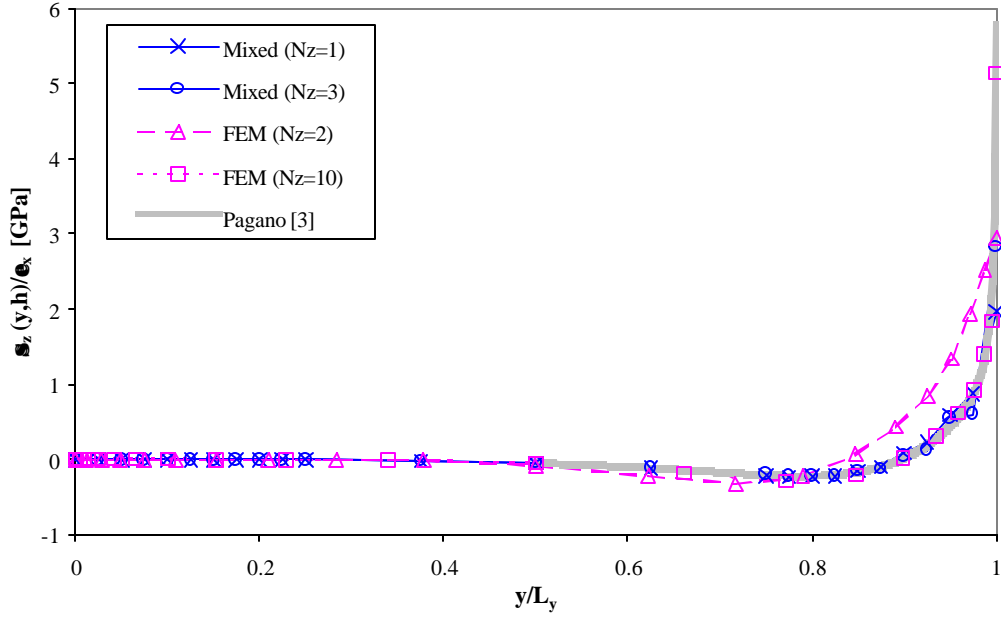
(b) Distribution of $\mathbf{s}_z$ along [0/90] interface ($z = h$)

Figure 4. Stress and Displacement Results for Flat Laminated Composites.
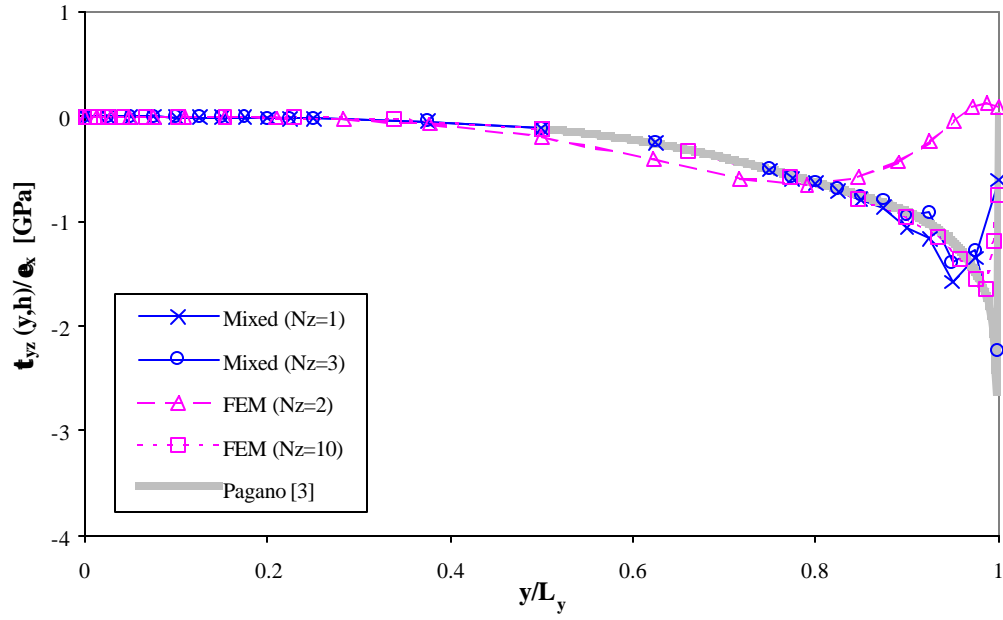
(c) Distribution of t_{yz} along [0/90] interface ($z = h$)
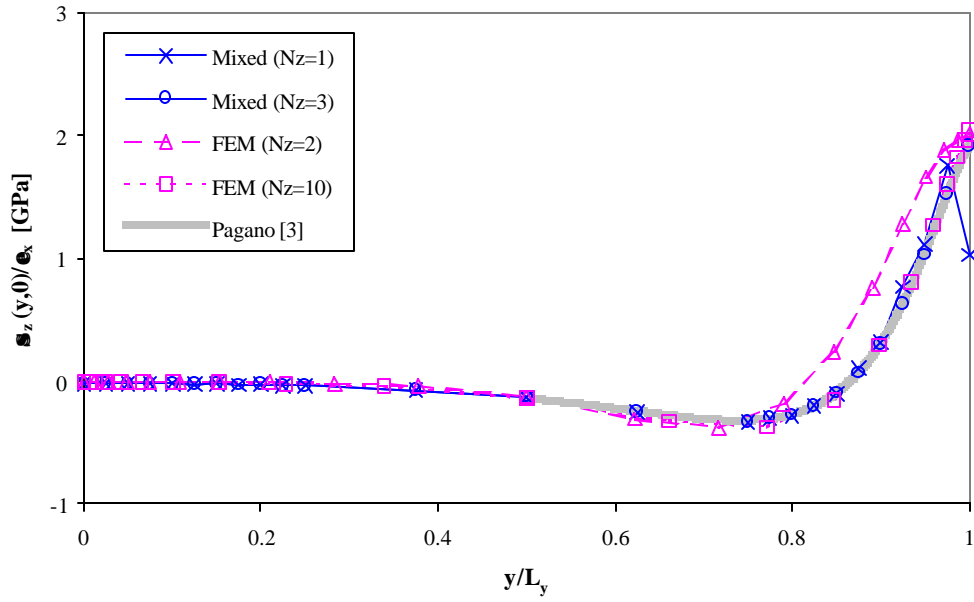
(d) Distribution of s_z along central plane ($z = 0$)

Figure 4. Stress and Displacement Results for Flat Laminated Composites (concluded).

While the analytic solution yields zero shear stress with a high peak at the free edge ($y = L_y$), the present and FEM solutions give finite values, as Figure 4 (c) shows. This is because the linear shape functions used in both finite element methods are not accurate enough to capture the drastic stress change at the free edge. Although the increment of the sublayer in the present mixed method makes the peak value higher, it creates wiggles in the shear-stress distribution near the free edge. This is because the high stress gradient at the free edge influences the stress field inside the edge. As pointed out earlier, the excessive continuity for stresses should be avoided at singularities and at abrupt material property change interfaces. Therefore, the penalty method is more suitable than the irreducible formulation because it can relieve the excessiveness by controlling the penalty parameter for the stress constraint condition (a_2). Note that in this case of such an extremely high stress gradient, even the penalty method cannot cure the problem completely.

The normal stress at the central surface [Figure 4 (d)] with one sublayer shows good agreement with the analytic solution except for a hump at the free edge. This hump does not appear with three sublayer solutions.

1.3.2   RVE of Woven Fabric Composites

The RVE of the model is divided into several subregions; each subregion is occupied by a characteristic fabric yarn or a matrix (see Figure 5). The L_x and L_y variables represent the length of RVE in the x- (warp) and y- (fill) directions, and t_w and t_f half of the thickness of the warp and fill yarn, respectively. The yarn is assumed as transversely isotropic, and the matrix as isotropic materials. Each yarn and the matrix subregion of the RVE are discretized into several finite elements in the longitudinal and transverse directions. The N_x and
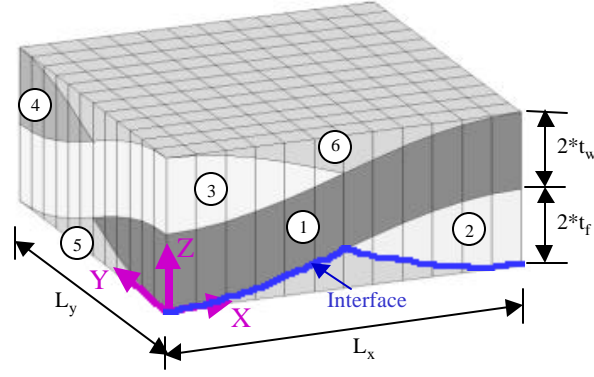
Figure 5. Representative Volume Element of a Plain-Weave Composite. Numbers in circles indicate the numbers of subregions.

N_y variables represent the numbers of subdivisions in half of the length of RVE in the x- and the y- directions ($L_x/2$ and $L_y/2$), respectively.

The cross-sectional boundary of the yarn is confined by $h_L = h_1$ (lower boundary) and $h_U = h_2$ (upper boundary). Because of yarn waviness and the elliptical cross-sectional boundary of the yarns, h_L and h_U are functions of both x and y. Yarn waviness at each subregion is assumed to be sinusoidal functions. Lower and upper surface coordinates of the yarn subregions are as follows:

$$h_L^{(1)} = t_f \left(1 - \cos\frac{px}{L_x}\right) + t_w \left(1 - \cos\frac{py}{L_y}\right) \quad , \quad h_U^{(1)} = t_f \left(1 - \cos\frac{px}{L_x}\right) + t_w \left(1 + \cos\frac{py}{L_y}\right)$$

$$h_L^{(2)} = t_f \left(1 + \cos\frac{px}{L_x}\right) + t_w \left(1 - \cos\frac{py}{L_y}\right) \quad , \quad h_U^{(2)} = t_f \left(1 - \cos\frac{px}{L_x}\right) + t_w \left(1 - \cos\frac{py}{L_y}\right)$$

$$h_L^{(3)} = t_f \left(1 - \cos\frac{px}{L_x}\right) + t_w \left(1 + \cos\frac{py}{L_y}\right) \quad , \quad h_U^{(3)} = t_f \left(1 + \cos\frac{px}{L_x}\right) + t_w \left(1 + \cos\frac{py}{L_y}\right)$$

$$h_L^{(4)} = t_f \left(1 + \cos\frac{px}{L_x}\right) + t_w \left(1 + \cos\frac{py}{L_y}\right) \quad , \quad h_U^{(4)} = t_f \left(1 + \cos\frac{px}{L_x}\right) + t_w \left(1 - \cos\frac{py}{L_y}\right)$$

(42)

where a superscript indicates the subregion number. Lower and upper surface coordinates of the bottom and top matrix subregions are as follows:

(1) for bottom matrix subregion (subregion 5),

$h_L^{(5)} = 0$, and

$$
h_U^{(5)} = \begin{cases}
t_f(1-\cos\dfrac{px}{L_x}) + t_w(1-\cos\dfrac{py}{L_y}) & \text{for } 0 \le x \le L_x/2 \,,\, 0 \le y \le L_y/2 \\[2ex]
t_f(1+\cos\dfrac{px}{L_x}) + t_w(1-\cos\dfrac{py}{L_y}) & \text{for } L_x/2 \le x \le L_x \,,\, 0 \le y \le L_y/2 \\[2ex]
t_f(1-\cos\dfrac{px}{L_x}) + t_w(1+\cos\dfrac{py}{L_y}) & \text{for } 0 \le x \le L_x/2 \,,\, L_y/2 \le y \le L_y \\[2ex]
t_f(1+\cos\dfrac{px}{L_x}) + t_w(1+\cos\dfrac{py}{L_y}) & \text{for } L_x/2 \le x \le L_x \,,\, L_y/2 \le y \le L_y
\end{cases}
\tag{43}
$$

(2) for top matrix subregion (subregion 6),

$$
h_L^{(6)} = \begin{cases}
t_f(1+\cos\dfrac{px}{L_x}) + t_w(1+\cos\dfrac{py}{L_y}) & \text{for } 0 \le x \le L_x/2 \,,\, 0 \le y \le L_y/2 \\[2ex]
t_f(1-\cos\dfrac{px}{L_x}) + t_w(1+\cos\dfrac{py}{L_y}) & \text{for } L_x/2 \le x \le L_x \,,\, 0 \le y \le L_y/2 \\[2ex]
t_f(1+\cos\dfrac{px}{L_x}) + t_w(1-\cos\dfrac{py}{L_y}) & \text{for } 0 \le x \le L_x/2 \,,\, L_y/2 \le y \le L_y \\[2ex]
t_f(1-\cos\dfrac{px}{L_x}) + t_w(1-\cos\dfrac{py}{L_y}) & \text{for } L_x/2 \le x \le L_x \,,\, L_y/2 \le y \le L_y
\end{cases}
\tag{44}
$$

and $h_U^{(6)} = 2(t_f + t_w)$.

The following boundary conditions are prescribed to simulate a tensile loading subject to a uniform displacement in the *x*-direction with lateral constraint in the *y*-direction. The zero vertical displacement at *z=0* simulates a case in which two RVEs are symmetrically stacked, as shown in the following equation:

$$u_1^{(k)}(0, y, z) = u_2^{(k)}(0, y, z) = 0 \quad , \quad \bar{u}^{(k)}(0, y, z) = u*^{(k)}(0, y, z) = 0$$

$$u_1^{(k)}(L_x, y, z) = u_2^{(k)}(L_x, y, z) = U_o \quad , \quad \bar{u}^{(k)}(L_x, y, z) = u*^{(k)}(L_x, y, z) = \frac{U_o}{2}$$

$$v_1^{(k)}(x, 0, z) = v_2^{(k)}(x, 0, z) = v_1^{(k)}(x, L_y, z) = v_2^{(k)}(x, L_y, z) = 0 \tag{45}$$

$$\bar{v}^{(k)}(x, 0, z) = v*^{(k)}(x, 0, z) = \bar{v}^{(k)}(x, L_y, z) = v*^{(k)}(x, L_y, z) = 0$$

$$w_1^{(k)}(x, y, 0) = 0$$

Figure 6 (a) shows a deformed shape under the above boundary conditions. The top surface of the RVE is twisted because of its antisymmetric geometry in the x- and y-directions. Figure 6 (b) shows the antisymmetric distributions of the vertical displacement at the intersection of the top surface and the xz-planes at $y = 0$ and $y = L_y$.

The thickness of the matrix subregions (subregions 5 and 6) at four corner points is zero according to the model. Physically, the lower (w_1) and upper (w_2) vertical displacements at these corners should be the same. However, because of the numerical errors, they do not match with each other with the coarse meshes ($N_x < 3$), as in Figure 6 (c). Therefore, finer meshes ($N_x \geq 4$) should be used to achieve the interfacial continuity, and $N_x = 6$ is chosen in this study.

While one displacement penalty parameter is set as $\boldsymbol{a}_1 = 10^3$, two stress penalty parameters are chosen as $\boldsymbol{a}_2 = 10^2$ and $\boldsymbol{a}_2 = 0$ for a sensitivity study. The latter case ($\boldsymbol{a}_2 = 0$) means no stress constraint condition is enforced. Figure 6 (d) shows that the vertical displacement distributions are almost identical with two different $\boldsymbol{a}_2$, which indicates that the stress continuity condition has a negligible influence on the displacement results.

(a) Deformed shape ($N_x = 6$)

(b) Vertical displacements at top surface

(c) Convergence of model ($a_2 = 100$)

(d) Vertical displacements with two a_2
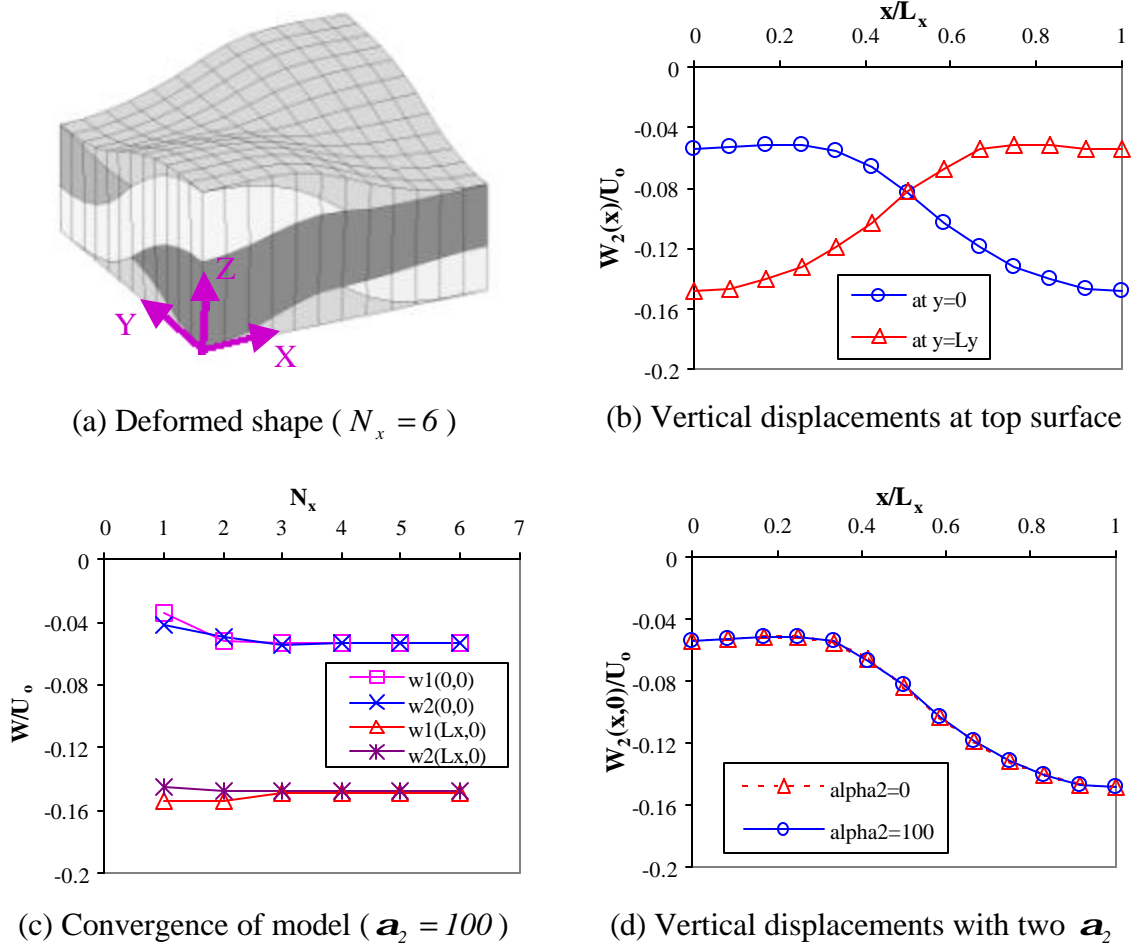
Figure 6. Displacement Results of RVE of Woven Composites.

Figure 7 shows the normal and shear stress distributions along an interfacial line

in Figure 5. These interfacial stresses are the local ones described in equation (4), which are

transformed from the stress components in the global coordinate system by the slopes of the

interfacial surfaces. The subscript (k) indicates the bottom matrix subregion (subregion 5), and

(l) indicates the upper yarns lying on top of the matrix (i.e., subregion 1 at $0 \le x \le L_x/2$ and

subregion 3 at $L_x/2 \le x \le L_x$). Figure 7 (a) and (b) show that the interfacial normal stresses

from the lower and the upper subregion agree well with each other, with only one sublayer in the

thickness (z) direction. The normal stress continuity can be achieved well even without the stress
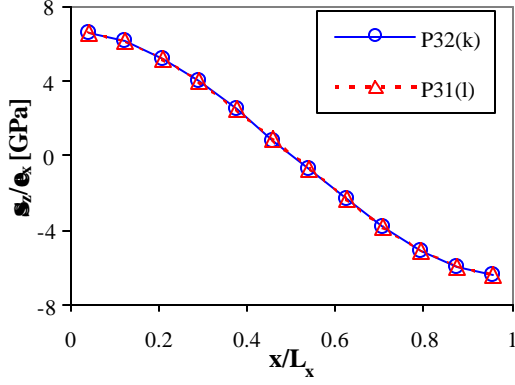
(a) Normal stress ($\boldsymbol{s}_z$) with $\boldsymbol{a}_2 = 100$
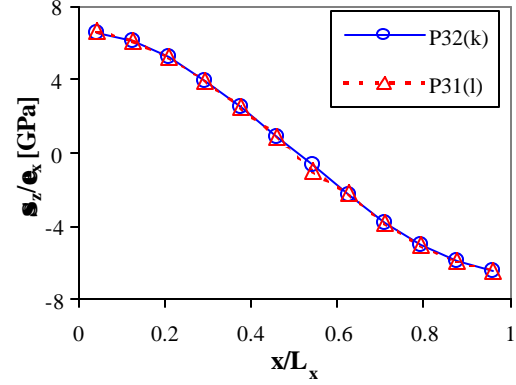
(b) Normal stress ($\boldsymbol{s}_z$) with $\boldsymbol{a}_2 = 0$
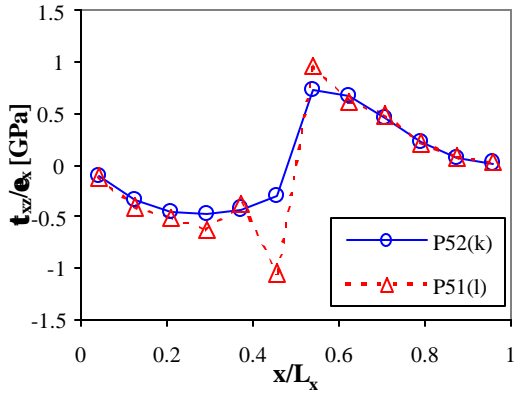
(c) Shear stress ($\boldsymbol{t}_{xz}$) with $\boldsymbol{a}_2 = 100$
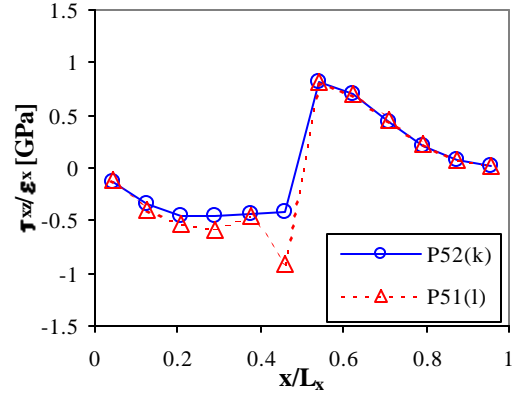
(d) Shear stress ($\boldsymbol{t}_{xz}$) with $\boldsymbol{a}_2 = 0$

Figure 7. Interfacial Normal and Shear Stress Distributions of RVE of Woven Composites with Two Different Penalty Parameters for Stress Continuity Condition.

constraint condition ($\boldsymbol{a}_2 = 0$). It also shows a smooth transition of the stress distribution with a significant change in the material properties at $x = L_x/2$.

Figure 7 (c) and (d) show that the interfacial shear stress continuity is achieved fairly well with the present method, except the region near $x = L_x/2$, where the high stress gradient is observed. The reason for the high stress gradient in the local shear stresses is that the local shear stresses ($\hat{\boldsymbol{s}}_4$ and $\hat{\boldsymbol{s}}_5$) are highly affected by the global axial stresses ($\boldsymbol{s}_1$ and $\boldsymbol{s}_2$) as indicated in equation (4), and these axial stresses change abruptly with the change in the material

properties at this region. The interfacial shear stresses do not match well at this region because the thickness of subregion 3 is zero at $x = L_x/2$. While two subregions (subregions 5 and 1) are considered in calculating the interfacial stresses at the left side of $x = L_x/2$, three subregions (subregions 5, 3 and 1) are considered in the calculation at the right side because of the zero thickness of subregion 3. Therefore, the stress continuity condition becomes,

(1) at left side of $x = L_x/2$,

$$\hat{P}_{42}^{(5)} = \hat{P}_{41}^{(1)} \quad \text{and} \quad \hat{P}_{52}^{(5)} = \hat{P}_{51}^{(1)} \tag{46}$$

(2) at right side of $x = L_x/2$,

$$\hat{P}_{42}^{(5)} = \hat{P}_{41}^{(3)} = \hat{P}_{42}^{(3)} = \hat{P}_{41}^{(1)} \quad \text{and} \quad \hat{P}_{52}^{(5)} = \hat{P}_{51}^{(3)} = \hat{P}_{52}^{(3)} = \hat{P}_{51}^{(1)} \tag{47}$$

where $\hat{P}_i^{(k)}$ is the local component of the interfacial stresses at the k-th subregion. However, it is hard to satisfy such a continuity condition with the zero thickness because of the numerical error in evaluating the stress components. The numerical error in the axial stresses, whose magnitudes are much larger than those of the shear stresses, affects the interfacial shear stresses significantly, so that jumps and mismatches are observed at this region.

Figure 7 (c) and (d) also show that the shear stress distribution is smoother without the stress constraint condition ($a_2 = 0$) than $a_2 = 100$. As observed in the flat-laminated case, the excessive stress continuity conditions are not necessary in the present mixed method, and should be avoided at the stress singularity or the material mismatch. Not shown on the figure are the results for $a_2 \gg a_1$, which make a little improvement in the stress continuity but cause the displacement results to be unrealistic and far different from the one in Figure 6 (a).

1.3.3 Effective Elastic Moduli of Plain-Weave Laminates

Zhang and Harding [7] used a strain energy equivalency principle to predict the elastic properties of a plain-weave composite. The finite element method was used to evaluate the strain energies. They applied this method to a one-directional undulation model in the loading direction only. Comparisons were made with experimental data for a plain-weave carbon epoxy laminate [8]. Because of the one-dimensional model, discrepancies occurred for the in-plane shear modulus ($\overline{G}_{xy}$) and the properties in the transverse direction ($\overline{E}_y$ and $\overline{\boldsymbol{n}}_{xy}$).

Naik and Ganesh [9] suggested two refined models, slice array model (SAM) and element array model (EAM), and also suggested modifications of the existing simple models, modified mosaic parallel model (MMPM) and modified Kabelka's model (MKM). These models predicted two-dimensional elastic properties, considering the actual yarn cross-section geometry, possible gap between two adjacent yarns, and undulation and continuity of yarns along both warp and fill directions. The effective moduli are calculated by the various models for plain-weave composites with E-glass/epoxy and carbon/epoxy materials.

Figure 8 (a) shows an RVE of the present model with the maximum yarn thickness (a) and the wavelength of the yarn ($\boldsymbol{l}$), whose ratio ($a / \boldsymbol{l}$) represents the waviness ratio. The overall volume fraction filled with yarn subregions in the RVE is approximately 0.64. The moduli agree fairly well with both the experimental and the numerical results for various waviness ratios, as shown in Figure 8. Not plotted in the figure, the present method can calculate three-dimensional moduli and Poisson's ratios, such as $\overline{E}_z$, $\overline{G}_{xz}$, $\overline{G}_{yz}$, $\overline{\boldsymbol{n}}_{xz}$ and $\overline{\boldsymbol{n}}_{yz}$, as opposed to the existing two-dimensional methods.

(a) RVE and dimension

(b) Ishikawa [8] (a/ λ=0.025)

(c) Naik [9]: E-glass/epoxy (a/ λ =0.075)

(d) Naik [9]: carbon/epoxy (a/λ=0.035)
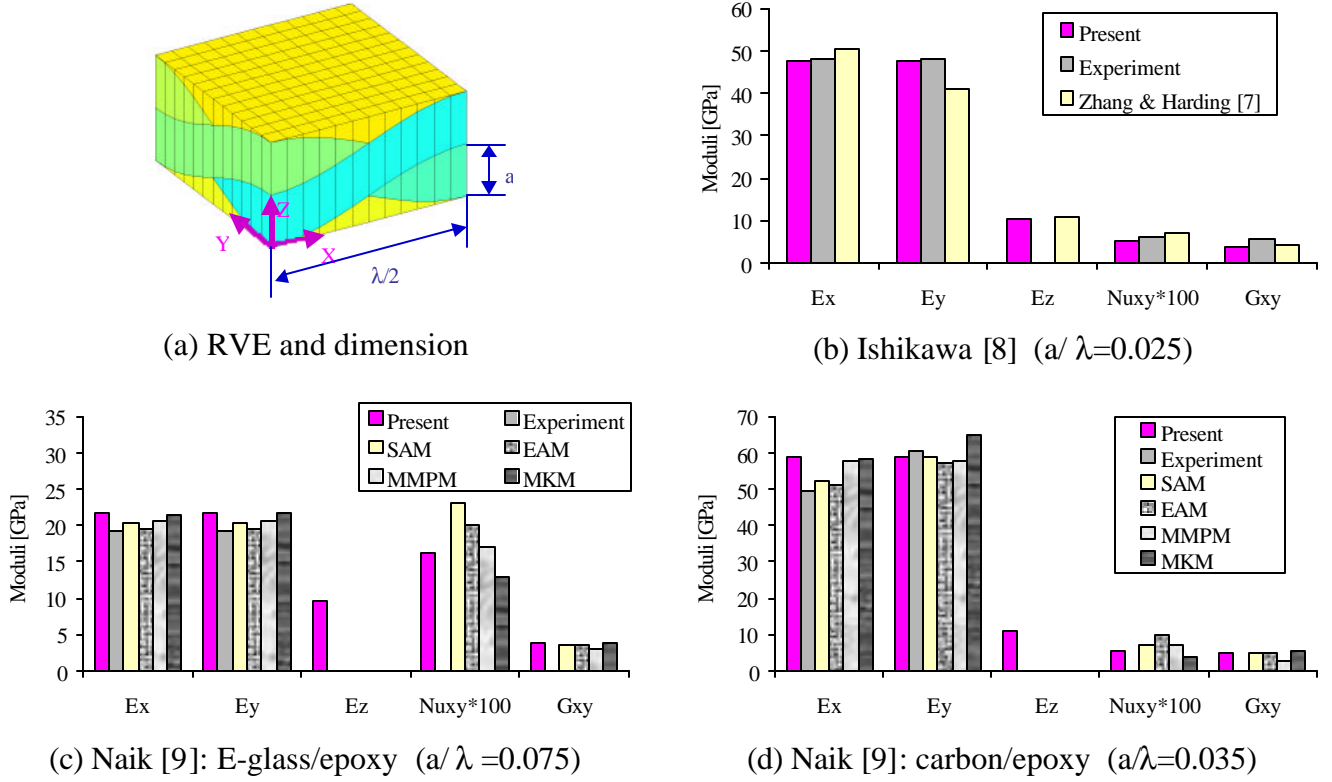
Figure 8. Comparison of Numerical Prediction of Effective Elastic Moduli with Existing Results.

1.3.4   Failure Analysis of Model Laminated Composites

In situ damage observation is made with flat and model laminates containing one-directional yarn crimping [10]. Test specimens were loaded in tension in the *x*-direction (warp direction) in a portable load frame placed on a microscopic stage. Laminates were made from AS4/3501-6 graphite/epoxy unidirectional prepreg, whose properties are listed in Table 2 [11]. The present numerical prediction is compared with the experimental results for a cross-ply flat laminate, $[90/0]_{2s}$, and a model laminate, $([90_2/0_2]_s , [0_2/90_2]_s , 0.050)$. The notation used for the model laminate indicates the lamination sequence away from the wavy region, midsection lamination sequence of the wavy region and the waviness ratio, respectively. The hygrothermal conditions of $\Delta T = -95\,^{\circ}C$ and *c*=0.005 are used in the calculation.

Table 2
Three-Dimensional Properties of Unidirectional AS4/3501-6 Composite

Engineering Constants								
E_x	E_y	E_z	$\boldsymbol{n}_{xy}$	$\boldsymbol{n}_{xz}$	$\boldsymbol{n}_{yz}$	G_{yz}	G_{xz}	G_{xy}
[GPa]						[GPa]		
138	10	10	0.3	0.3	0.53	2.9	5.5	5.5
Strength Data [MPa]								
Tension			Compression			Shear		
X_x^T	X_y^T	X_z^T	X_x^C	X_y^C	X_z^C	S_{yz}	S_{xz}	S_{xy}
1930	52	52	1450	210	258	103	93	93

In both the flat and woven cases, the first-ply-failure (FPF) occurs at the 90° fill yarns in the form of transverse matrix cracking. In the flat laminate, the maximum stress occurs at $y = L_y$ because of the singularity in $\boldsymbol{s}_x$ at the free edge. The stress distribution in the y-direction is calculated with the present method and compared with an analytic solution obtained by a method suggested by Pagano [3], as Figure 9 shows. The figure clearly shows the singularity at the free edge. Similar distribution is observed in the woven model laminates. Therefore, fine meshes are required near the free edge for an accurate failure prediction.
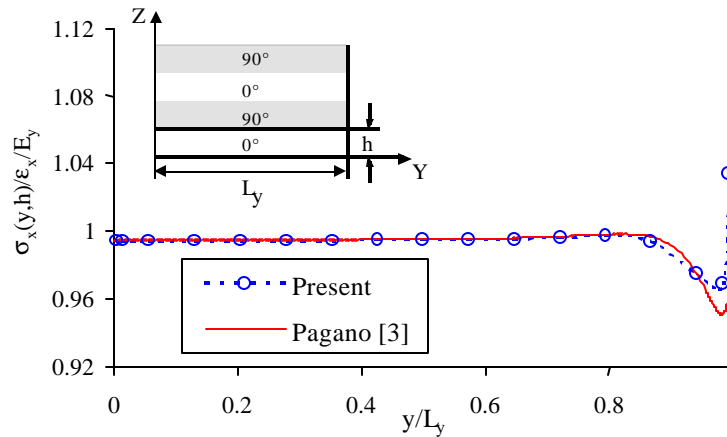

Figure 9. $\acute{o}_x$ Distribution in y-Direction at an Interface between Lower 0° and Lower 90° Ply.

In the model laminates, the calculated stress distribution in the *x*-direction shows that the maximum stress occurs at the upper fill-yarn near the crimping at $x = 0.57\,L_x$. The calculated location agrees well with the *in situ* observation of the first matrix cracking, as Figure 10 shows.

First crack at y=0.54 L$_y$
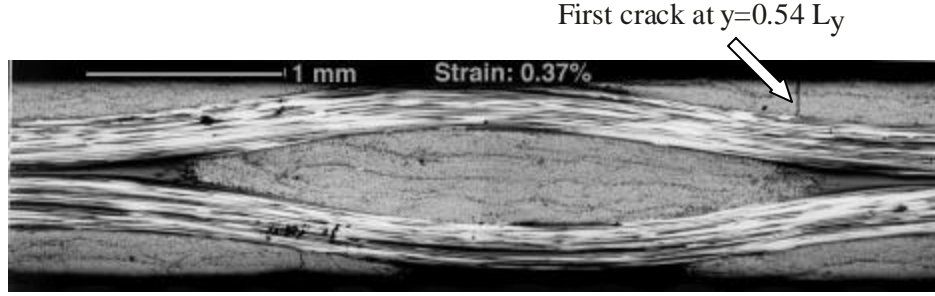
Figure 10. Cross Section of Woven Model Laminate when the First Cracking is Observed [10].

A primitive progressive damage model is achieved by degrading transverse yarn modulus with a matrix degradation factor of $E_m^* = 0.2$. The last-ply-failure (LPF) occurs at the 0° warp yarns in the form of fiber breakage. The strengths at FPF and LPF are plotted in Figure 11 with fairly good agreement with the experiment. The Tsai-Wu quadratic failure criterion provides more conservative and better results than the maximum stress criterion because the former considers interactions between the stress components. However, the maximum stress criterion is useful to identify the critical stress component for the damage mode prediction.

1.4   SUMMARY

Three-dimensional displacements and stresses are analyzed numerically based on Reissner's mixed variational principle. The three-dimensional model is treated semi-two-dimensionally by making an assumption on the interlaminar stress variations and integrating the variational energy in the thickness direction. Additional energy terms are added to the
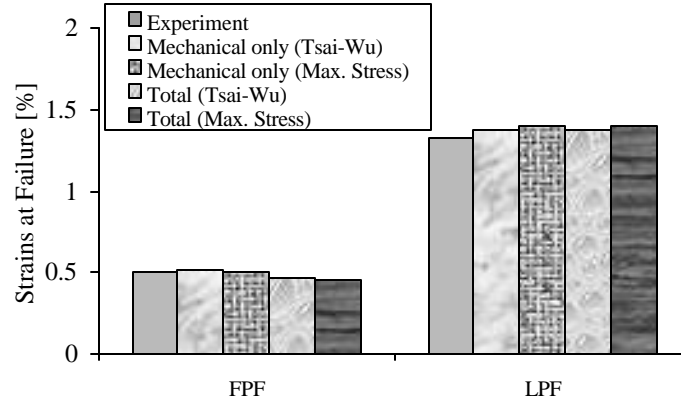
(a) Flat: ($[90/0]_{2s}$)
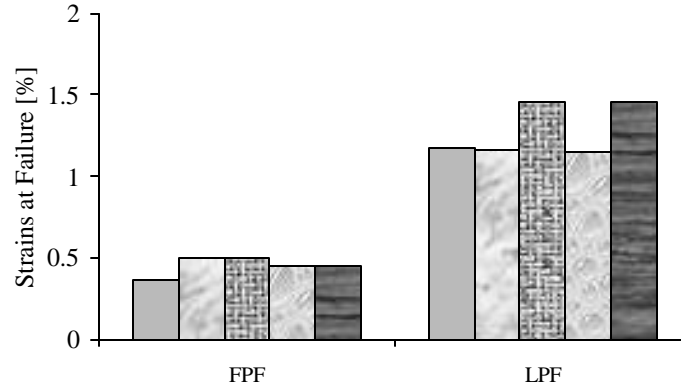
(a) Woven: ($[90_2/0_2]_s$, $[0_2/90_2]_s$, 0.050)

Figure 11. Numerical Prediction of Strains at FPF and LPF. Total strain is a sum of mechanical and residual strains.

variational energy to impose the displacement and stress continuity at the interface by the penalty approach. Two penalty parameters are employed to enforce the displacement and the stress continuity conditions, respectively. The Rayleigh-Ritz approximation with polynomial shape functions yields a system of linear equations by taking derivatives of the variational energy equation with respect to the independent unknown variables.

The present method is applied to analyze flat laminated composites with a free edge and the RVE of the plain-weave composites. The results are compared and validated with the displacement-based FEA and/or analytic solution. Since the stresses are evaluated pointwise

without any interpolation of the displacement results, more accurate interlaminar stresses are obtained at the interfaces between two different materials with few sublayers compared with the displacement-based FEA.

The interfacial normal and shear stress continuity is achieved well with the penalty approach, except in the region in which the thickness of the subregions is small. It is found that the imposition of the displacement continuity condition is more important than that of the stress continuity condition. Furthermore, the excessive continuity condition in the stress fields is not necessary and may induce convergence instability in the data of the displacement as well as the stress fields. Imposing only the displacement constraint without the stress constraint yields a smoother interfacial normal and shear stress distribution than the case that considers both constraint conditions.

The reliable stress calculation is used to predict the effective elastic moduli. The numerical calculation with the present model of the RVE shows good agreement with previous experimental and numerical results made for both flat and woven laminated composites with various yarn-waviness ratios. Since the present method calculates the three-dimensional elastic moduli with three-dimensional geometry, it can be used not only for the 2-D but also for 3-D woven composites.

Discrete damage analysis is achieved with the reliable prediction of the stress field with the existing failure criteria. The failure analysis includes residual stress calculation to consider hygrothermal effects. The damage analysis results in a good prediction of the magnitude and location of the failure. A primitive progressive damage analysis is established by degrading the material properties of the damaged yarns to predict the final failure beyond the FPF.

With the presence of stress singularity at the free edge, the numerical calculation becomes mesh-dependent. Therefore, it is desirable to eliminate the singularity or reduce the dominance of the singular stresses in order to study the effect of the yarn crimping on the failure of the woven composites. Non-straight-edge specimens, such as a cruciform, can be used for this purpose to make the most of the stresses carried not by the edges but by the middle of the specimen.

1.5   CONCLUSIONS AND RECOMMENDATIONS

We have developed a three-dimensional model for the three-dimensional stress analysis of woven fabric composites. The model yields an accurate three-dimensional displacement and stress solution of woven fabric composites under any of the in-plane and the out-of-plane loading conditions including, but not limited to, extension, bending and twisting. The model can obtain the three-dimensional effective stiffness matrix for woven composites that a designer can plug into for finite element structural analysis. The model can also make an accurate damage prediction for woven composites through accurate in-plane and interlaminar stress calculations.

This present mixed formulation offers better accuracy at high stress gradients over the current state-of-the-art displacement-based method. However, by introducing more variables, this new method becomes resource-intensive in terms of computer memory and computational time. A future effort will be made to develop a model based on the displacement-based method to make the computation economical and efficient.

2. ANALYTICAL CHARACTERIZATION OF GRAPHITIC FOAMS

2.1 INTRODUCTION

In recent years, there have been an increasing number of applications requiring lightweight and more efficient thermal management, such as high-density electronics, hybrid diesel-electric vehicles, communication satellites, and advanced aircraft. The primary concerns in these thermal management applications are high thermal conductivity, low weight, low coefficient of thermal expansion, high specific strength, and low cost [12]. Carbon foam was shown to demonstrate numerous unique properties that make it an attractive material for use of low-cost, lightweight, insulating, energy-absorbing structural components. Unique properties of the carbon foam material include [13]:

(1) Precursors: coal extracts are inexpensive (less than $0.10 per kg) and readily available.

(2) Manufacturing of the foam can be readily scaled up by continuous extrusion of constant cross-section parts, or net-shape batch production of special shapes. Required manufacturing equipment is commercially available; projected finished material cost is less than $14 per kg.

(3) Low bulk thermal conductivity: less than 1.0 W/mK, but potential for high thermal conductivity if the foam is converted to graphite through heat treatment at >2000°C.

(4) Fire resistance: once carbonized at >1000°C, the foam does not contain a sufficient volatile material with which to support combustion.

(5) It will not give off noxious or hazardous fumes when heated.

(6) Its properties can be readily engineered to meet different requirements. By varying the processing conditions, the density, compressive strength, and ability to absorb energy can be tailored to meet specific requirements.

(7) Integration with other materials: examples include impregnation with phenolic or other resins, lamination with Kevlar tape, and lamination with a phenolic-resin skin. Attaching fiber-reinforced polymer or metallic facesheets allows joining to other components by more conventional methods, protects the foam from localizing damage or abrasive wear, and transfers loads uniformly to the foam.

(8) Machinability: easily cut, milled, turned, etc., with conventional equipment and tooling.

(9) Formability: foam assumes shape of mold in batch operation and may be continuously formed.

(10) Joining: using a coke fusion process. This feature enables foams with different mechanical, thermal or electrical conductivity properties to be joined to produce a highly tailorable, anisotropic, sandwich material, as well as to allow repair to damaged structures.

(11) Impact absorption: carbon foam performs better than conventional polyurethane foams that are currently used extensively for impact absorption in aircraft.

(12) Additional improvement: additives such as chopped fibers, nanofibers or nanotubes, and crushed calcined cokes can add significantly to the strength and tailorability of the foams; unidirectional expansion of the foam and the orientation of fibers within the matrix enable the production of anisotropic foams with directional properties.

The carbon foam macroscopically possesses an isotropic material property. However, a microstructure of an open-cell foam possesses a pentagonal dodecahedron structure of the foam ligaments oriented approximately $109.47°$ with each other. The microstructure of foams reflects their method of preparation, which usually involves a continuous liquid phase that eventually solidifies. Surface tension and the elementary features of the liquid foam structure, which are

required to minimize surface energy during the foaming process (i.e., bubble nucleation process), results in three films that always meet at equal angles of 120° to form a film junction region called a plateau border, and four plateau borders always join at the tetrahedral angle of $cos^{-1}(1/3) \approx 109.47°$ [14,15].

Because of the tetrahedral cell microstructure, the macroscopic properties, such as foam moduli and strengths, are critically influenced by the deformation characteristics of the cell ligaments. Therefore, to develop a basic understanding of the performance of open-cell foam materials, it is critical that the deformation and failure mechanism of the cell ligaments critically be studied.

Preliminary research reveals that the graphitic alignment of the cell ligaments varies along its longitudinal direction. Processing parameters, such as temperature, pressure, etc., determine the porosity and the graphitic alignment of the carbon foam, which in turn determine its geometries and material properties. Once a research effort investigates appropriate microstructural characterization techniques to correlate the foam microstructure with the processing parameters, the foam microstructural geometry and the material properties, including mechanical elastic moduli, Poisson's ratio and thermal conductivity, etc., will be used for the mechanical and thermal analysis.

Because of slenderness, each ligament can be considered as a beam, and the tetrahedral cell microstructure with four ligaments as a frame structure. The four beams are located in three-dimensional space. The cross section of the beam varies in size and material properties in the longitudinal direction along the ligament. Because of the complex geometry and anisotropic material properties, it is appropriate to perform the analysis numerically to obtain accurate displacement and stress field solutions of foams. The numerical analysis will predict

longitudinal and transverse displacements as well as rotations, and calculate the reliable stress

and strain distributions along the beam ligaments that are connected and located in the three-

dimensional space and are deformed under arbitrary loading conditions.

2.2   PRELIMINARY ANALYSIS OF FOAM MODEL

2.2.1   Generation of Unit Cell of Carbon Foam

Because of the randomness and complexity of the microstructure of the carbon

foam, it is difficult to consider every cell of the whole foam individually. Instead, an assumption

is made that one of the cells can represent a certain behavior of the whole foam structure. The

microstructural characterization of the representative cell ligaments will then be correlated with

the macroscopic bulk properties by a statistical approach. A series of databases will be collected

for various size and spatial orientation of the cell ligaments, as well as for the property variation

due to the graphic alignment along the longitudinal direction of the ligaments.

The first step in the structural analysis of the foam is to generate the geometry of

the unit cell of the foam systematically. The unit cell can be generated by manipulating

geometric entities, such as keypoints, lines, areas and volumes. The ANSYS package, a

commercially available finite element package, is used to manipulate those entities by adding,

subtracting or merging methods.

The first step is to create a cube with dimensions of $2a \times 2a \times 2a$ in x-, y- and z-

directions, as shown in Figure 12. The origin (point 1) is located in the center of the cube. The

second step is to select four corner points (e.g., points 3, 5, 6, 8 in Figure 12), which are located

diagonally with each other on the faces of the cube. Connecting the four corner points then

generates a tetrahedron, whose volume is $V_{Tetra} = 8/3 \cdot a^3$. This tetrahedron can be divided into

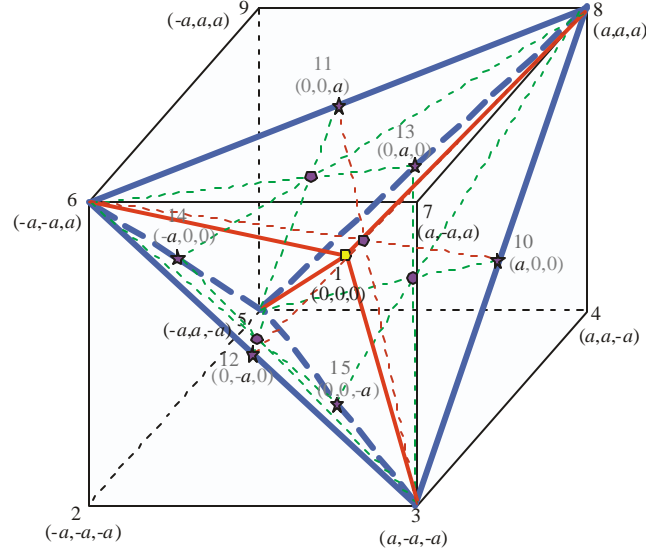four subtetrahedra that contain the origin (1-3-8-5, 1-8-6-5, 1-5-6-3 and 1-3-8-6). Local

Figure 12. Keypoints and Lines for Generating a Unit Cell of Carbon Foam.

coordinate systems, whose *x*-directions are parallel to the longitudinal directions of the

ligaments, are defined by using four lines that connect the keypoints (1-3, 1-5, 1-6 and 1-8). The

local coordinate systems are useful because the anisotropic material properties, with

consideration of the graphitic alignment, are input easily by defining the longitudinal directions

of the ligaments.

     The next step is to generate four spheres on the four corner points of the

tetrahedron. The spheres represent bubbles that are produced during the foaming process. The

radii of the spheres will determine the porosity of the unit cell of the foam. Figure 13 shows the

tetrahedron and the spheres.

     The next step is to subtract the spheres from the tetrahedron by geometric

manipulation. The remaining media is the unit cell of the foam. The volume of the unit cell

V_{Cell} is calculated automatically by the ANSYS. The porosity (f) of the foam is thus calculated

by $f = 1 - V_{Cell}/V_{Tetra}$. Figure 14 shows the unit cells with various porosities, and Figure 15

shows one of the ligaments of the unit cell of the foam at different view angles.
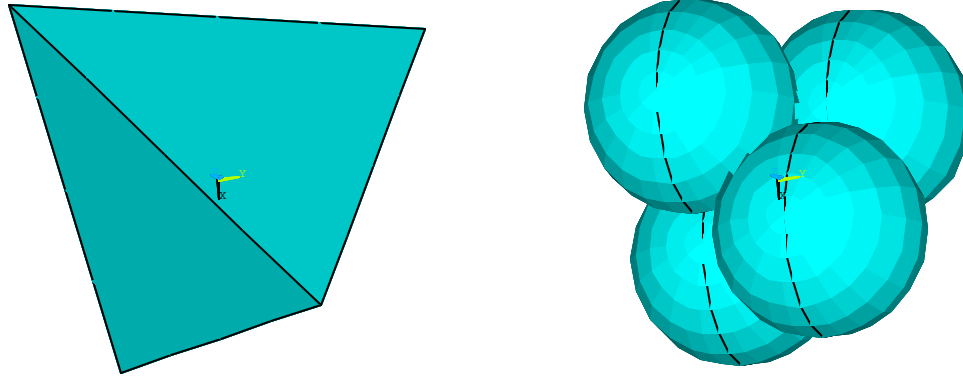
Figure 13. Tetrahedron and Spheres to Generate a Unit Cell of Carbon Foam.

(a) f = 10%   (b) f = 78%   (c) f = 98%
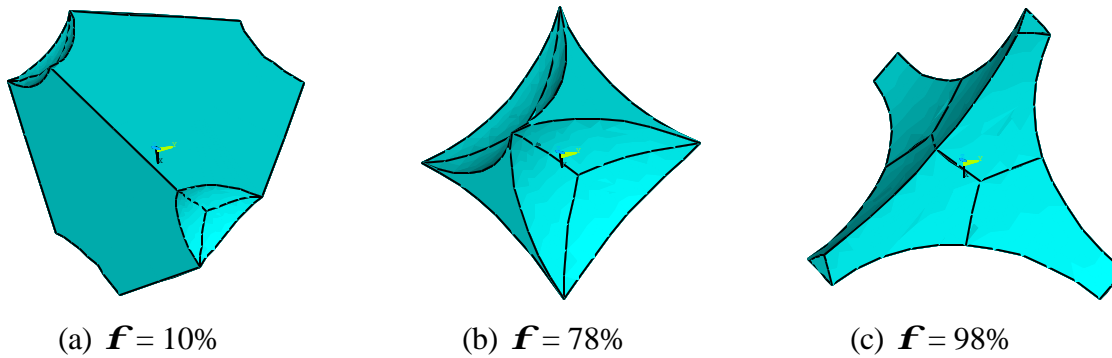
Figure 14. Unit Cells of Carbon Foam with Various Porosities.

For numerical analysis, it is advantageous to partition the ligaments along the longitudinal direc-

tions because of the varying material properties due to the graphitic alignment. It is then assumed

that material properties change segment by segment. The number of partitions will determine the

accuracy of the analysis. The ligament partitioning can be easily generated by manipulating the

tetrahedra at the beginning step. The tetrahedra can be duplicated and contracted, leaving the origin

in the same location. The unit cell with the partitioned ligaments is then generated by following the

same steps as generating the spheres and subtracting them from the partitioned tetrahedra

geometrically, as Figure 16 shows. By setting mesh parameters for a desired refinement, and

running an automatic mesh routine of ANSYS, three-dimensional tetrahedral finite elements are

automatically generated as shown in Figure 17.

Figure 15. A Ligament of a Unit Cell of Carbon Foam at Different View Angles.
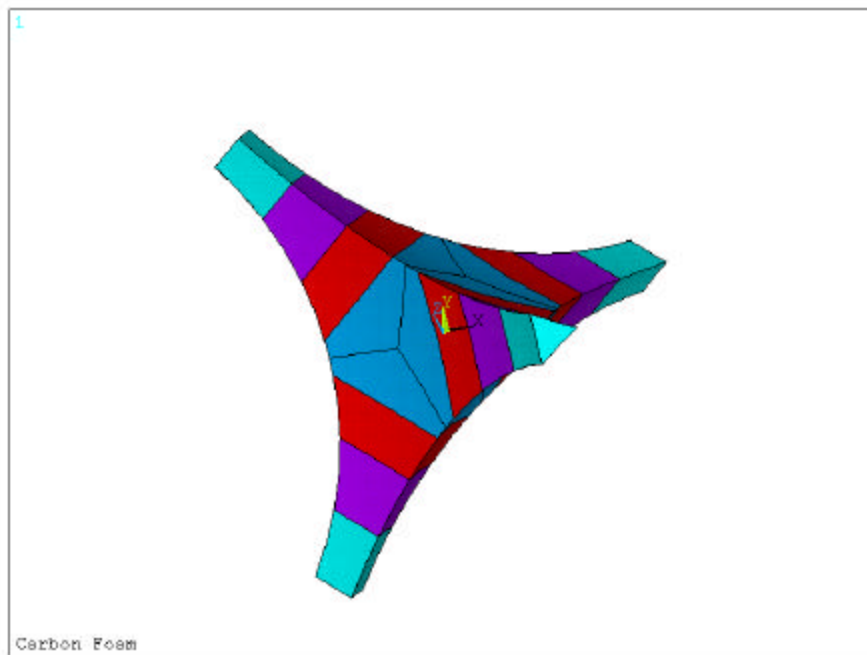
Figure 16. A Unit Cell of Carbon Foam Partitioned for Varying Material Properties Along Ligaments.
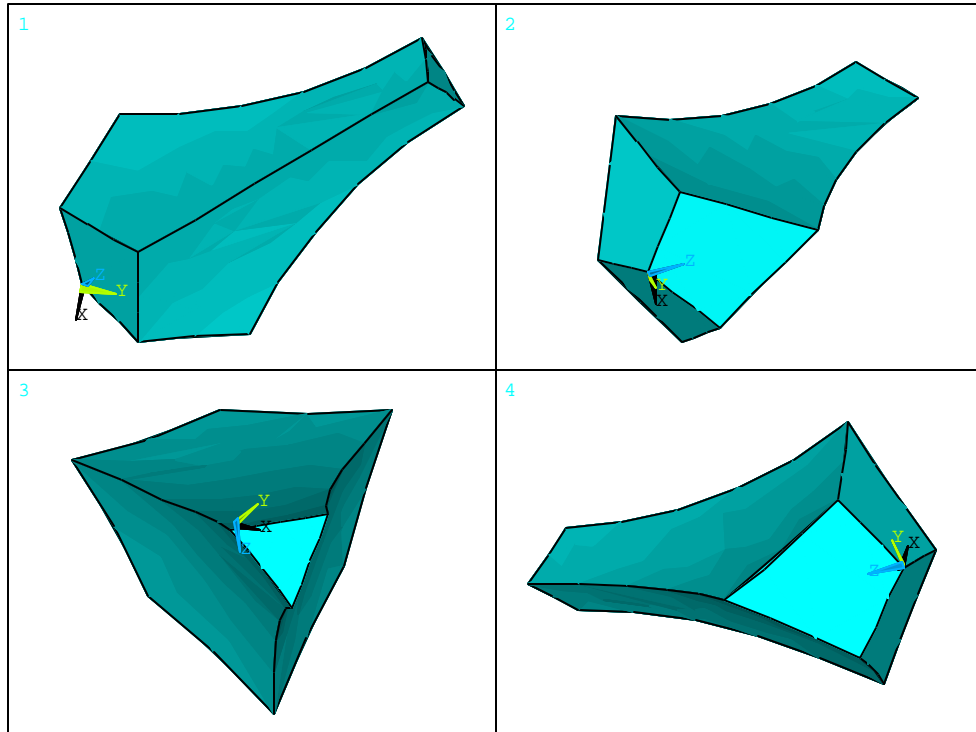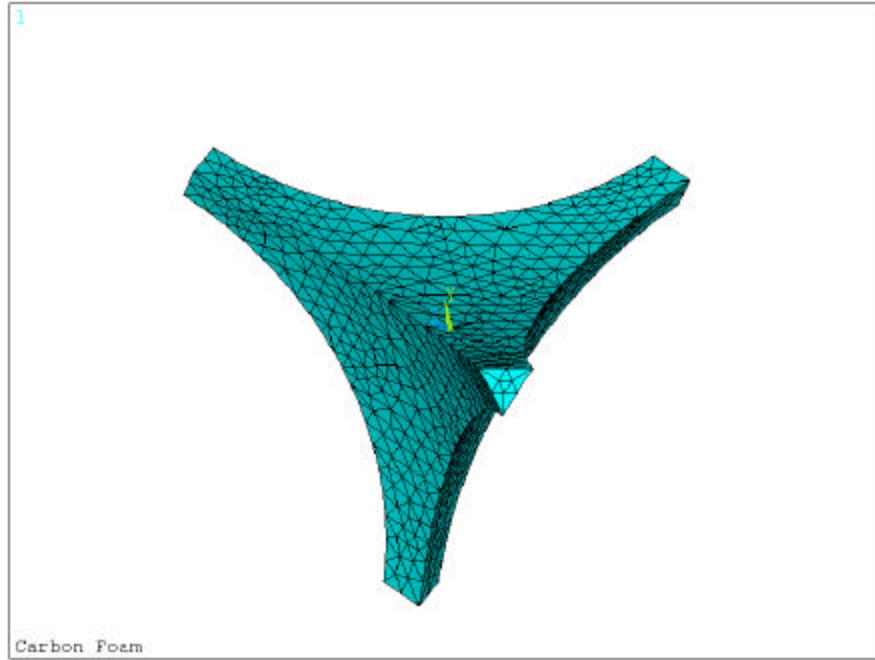
Figure 17. Finite Element Meshes for Unit Cell of Carbon Foam.

2.2.2   FEA

For the FEA, appropriate loading and boundary conditions should be specified on the unit cell of the foam. Under a certain loading condition, the carbon foam behaves according to overall material properties, such as bulk modulus and Poisson's ratio. The overall material properties can be assumed to be isotropic and can be measured experimentally, as suggested by existing methods [16]. For the analysis of the unit cell, we need to understand the relationship between the overall loading/boundary conditions (OBC) and the ligament boundary conditions (LBC). The LBC varies depending on the location, size and orientation of the unit cell under a certain OBC.

The LBC can be determined by the following bulk analysis. The first step is to generate an imaginary cube inside which a unit cell of the foam is located, as depicted in Figure 18. The imaginary cube can be generated by merging a cube and a unit cell geometrically by the

43
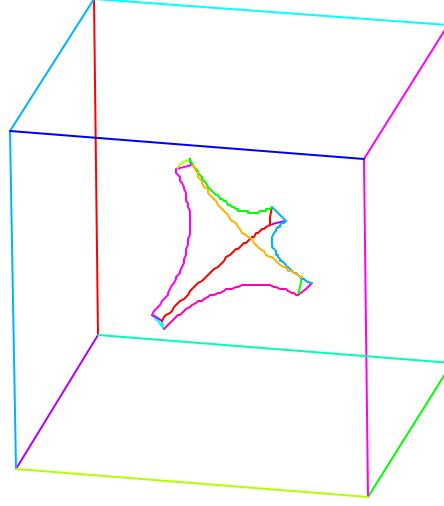
Figure 18. An Imaginary Cube Inside which a Unit Cell of the Foam is Located.

ANSYS. Overall loading and boundary conditions are then applied to the faces of the bulk cube. For a uniform loading condition, one of the faces is fixed and the opposite side is loaded, whereas the other four faces are free to deform. Under the OBC, the bulk cube deforms isotropically according to the bulk moduli and the Poisson's ratio, and the FEA calculates the deformations and stresses point by point. The LBC are then determined by the results on the points that coincide with the unit cell of the foam. The second FEA is run by assigning the recorded displacements to the unit cell as the LBC.

The current method is used for the moduli back-calculation of the carbon foam. Effective elastic moduli are calculated by solving six different cases under uniform axial and shear strain loadings ($\bar{e}_i$). For each uniform-strain boundary condition, effective stresses ($\bar{\boldsymbol{s}}_i$) are calculated by taking a volumetric average, as follows:

$$\bar{\boldsymbol{s}}_i = \frac{\int_V \boldsymbol{s}_i(x, y, z)\, dxdydz}{V} \quad , \quad (i = 1, \cdots, 6) \tag{48}$$

Components of 6×6 effective stiffness matrix ($[\bar{C}_{ij}]$) and effective compliance matrix ($[\bar{S}_{ij}]$) are then obtained by the following calculation:

44

$$\{\overline{\boldsymbol{s}}_i\} = [\overline{C}_{ij}]\{\overline{e}_i\} \quad \text{and} \quad [\overline{S}_{ij}] = [\overline{C}_{ij}]^{-1} \tag{49}$$

where

$$[\overline{C}_{ij}] = \begin{bmatrix} \overline{C}_{11} & \overline{C}_{12} & \overline{C}_{13} & \overline{C}_{14} & \overline{C}_{15} & \overline{C}_{16} \\ \overline{C}_{21} & \overline{C}_{22} & \overline{C}_{23} & \overline{C}_{24} & \overline{C}_{25} & \overline{C}_{26} \\ \overline{C}_{31} & \overline{C}_{32} & \overline{C}_{33} & \overline{C}_{34} & \overline{C}_{35} & \overline{C}_{36} \\ \overline{C}_{41} & \overline{C}_{42} & \overline{C}_{43} & \overline{C}_{44} & \overline{C}_{45} & \overline{C}_{46} \\ \overline{C}_{51} & \overline{C}_{52} & \overline{C}_{53} & \overline{C}_{54} & \overline{C}_{55} & \overline{C}_{56} \\ \overline{C}_{61} & \overline{C}_{62} & \overline{C}_{63} & \overline{C}_{64} & \overline{C}_{65} & \overline{C}_{66} \end{bmatrix} \tag{50}$$

Finally, the three-dimensional effective elastic moduli are calculated by the following:

$$\overline{E}_x = \frac{1}{\overline{S}_{11}}, \quad \overline{E}_y = \frac{1}{\overline{S}_{22}}, \quad \overline{E}_z = \frac{1}{\overline{S}_{33}}$$

$$\overline{G}_{yz} = \frac{1}{\overline{S}_{44}}, \quad \overline{G}_{xz} = \frac{1}{\overline{S}_{55}}, \quad \overline{G}_{xy} = \frac{1}{\overline{S}_{66}} \tag{51}$$

$$\overline{\boldsymbol{n}}_{xy} = -\frac{\overline{S}_{12}}{\overline{S}_{11}}, \quad \overline{\boldsymbol{n}}_{xz} = -\frac{\overline{S}_{13}}{\overline{S}_{11}}, \quad \overline{\boldsymbol{n}}_{yz} = -\frac{\overline{S}_{23}}{\overline{S}_{22}}$$

The overall effective moduli of the foam are then calculated by repeating the above procedure with various sizes and orientations of the unit cells in the three-dimensional space. A statistical approach can be used to handle a huge selection of random sizes and orientations.

2.3   SUMMARY

The emerging ultra-lightweight material, carbon foam, is modeled with the three-dimensional microstructures to develop a basic understanding of the performance of open-cell foam materials. The model will describe the deformation behavior accurately and will be used to investigate the failure mechanism of the cell ligaments.

Because of the randomness and complexity of the microstructure of the carbon foam, the representative cell ligaments are first characterized in detail at the microstructural level. The microstructural characterization will then be correlated with the macroscopic bulk properties by a statistical approach. A series of databases will be collected for various sizes and spatial orientations of the cell ligaments, as well as the property variation due to the graphic alignment along the longitudinal direction of the ligaments.

A computer program, "3D Foam," will be developed to predict longitudinal and transverse displacements as well as rotations, and calculate the reliable stress and strain distributions along the ligaments. Because of slenderness, each ligament can be considered as a beam, and the tetrahedral cell microstructure with four ligaments as a frame structure. The four beams are located in three-dimensional space under arbitrary loading conditions. The cross section of the beam varies in size and material properties in the longitudinal direction along the ligament. A tool integrating the process model along with the micro- and macro-analysis of the carbon foam will lead to an optimal process design to improve foam quality and to reduce cost.

2.4   CONCLUSIONS AND RECOMMENDATIONS

An analytic model was developed for the unit-cell of carbon foam utilizing variable material properties and ligament cross-section geometry, which are consistent with an open-cell foam. The model will be used to correlate the microstructural properties such as graphitic alignment, porosity and ligament structure with bulk properties that are being measured by mechanical tests. Experimental validation of the model has yet to be completed. The validation effort will include measurement of bulk materials properties and observation of ligament deformation using the miniature test fixture in the SEM.

3. MODEL DEVELOPMENT OF CARBON FOAM BLOWING PROCESS

3.1   LITERATURE REVIEW

Considerable literature research in theoretical and experimental areas was conducted on polymer foam formation processes [17-22]. Polymer foam can be produced by a wide variety of processes: expandable beads, injection molding, and extrusion. However, all of these processes have one basic phenomenon in common: the nucleation and subsequent nonisothermal growth of bubbles upon sudden supersaturation of a solution consisting of a gas dissolved in the melt polymer. This is similar to the carbon foam forming process. In the carbon foam blowing process, a gas dissolves or is trapped in the pitch under high pressure. As the high pressure releases, the bubbles in the supersaturated solution form, grow, and coalesce. The bubble walls between cells open up, which results in forming the open cells [23]. The current models of polymer foam processes are based on the following assumptions:

(1)   Nucleation

The nucleation in polymer foaming processes can be classified as two types: homogeneous and heterogeneous. The classical nucleation is used to describe the phenomena.

(2)   Foam bubble growth

(a) The bubble is spherical.

(b) The gas inside the bubble follows the ideal gas law.

(c) The gas concentration varies only with the radial position of the sphere and time. The relationship between the gas pressure in the bubble and the residual gas concentration on the liquid layer surrounding the bubble follows Henry's law.

(d) The melt polymer properties are independent of the gas concentration.

(e) Because the process is so quick, it can be considered as an isothermal process.

(f) The inertial effects are negligible.

(g) The melt polymer is considered as a Newtonian fluid.

(3) Mold filling

In the mold filling process, the mass and momentum conservation equations are used to simulate the process. As the thickness of a foam is usually much smaller than the length and width, the Hele-Shaw equation is often used to simplify the three-dimensional flow. As the bubbles grow, the foam volume increases (density of foam reducing) to fill the mold cavity.

3.2 RESEARCH APPROACH

Initially, homogeneous nucleation will be assumed in the model. The classical nucleation theory will be used in the model [24,25].

Most work in this research will focus on the bubble growth, because the bubble shape, size and distribution determine the foam properties [25-29]. The current models in the polymer foam process may be used for the initial bubble growth after modifying. However, they cannot be used for the carbon foam process that is an open-cell foam forming process. After the bubbles touch each other, the walls of the impinging bubble collapse. This forms the open-cell foam. In the fluid mechanics theory, the determination of the cell structure is a free-surface problem. This is quite a challenging topic because the location of the free surface is not known *a priori*, and the shape of the free surface influences the flow through a complicated nonlinear boundary condition, the normal-stress condition. When motion is steady or quasi-steady at a free surface between liquid and gas, the boundary conditions are as follows: (a) no flow normal to the surface, (b) no tangential stress on the surface if the surface tension gradients are negligible, and

48

(c) balancing of gas pressure, liquid pressure and normal viscous stress of the liquid with the

capillary pressure that is the product of the surface tension and mean curvature of the surface.

All iterative schemes employ a similar strategy. First a location of the free surface is chosen,

either by an informed guess or on the basis of the previous iterations. The governing equations

of mass and momentum are solved for the velocity and pressure fields in the liquid, but only two

of the three boundary conditions are satisfied. The residual in the third boundary condition is

used to decide how to alter the location of the free surface. The calculation process is repeated

until the calculation error is smaller than a criterion. This scheme is complex and time-

consuming because meshes have to be regenerated in the calculated domain at each calculation

step (one time step consists of many calculation steps), and convergence is often difficult to

obtain. On the other hand, the model used in polymer foam forming is much simpler than the

free-surface calculation. Although it may not be as accurate as the previous one, it can provide

basic information about the foam growth and process parameters. At this stage a similar method

in polymer foam-forming is used after modification. At the initial bubble growth, the

assumption of bubble spherical shape is acceptable, as the following calculation indicates:

$$\frac{dR}{dt} = \frac{(P_g - P_L)R}{4\mu} - \frac{\sigma}{2\mu}$$

$$\frac{d}{dt}\left(\frac{4\pi}{3} \frac{P_g R^3}{\Re T} \right) = 4\pi R^2 D \frac{\partial c}{\partial r}\bigg|_{r=R}$$

$$\frac{\partial c}{\partial t} + \frac{dR}{dt} \frac{R^2}{r^2} \frac{\partial c}{\partial r} = D \frac{1}{r^2} \frac{\partial}{\partial r}(r^2 \frac{\partial c}{\partial r})$$

The initial and boundary conditions are as follows:

$R(0)=R_I$

$P_g(0)=P_{g, i}$

$c(r,0)=c_i(r)$

$c(R,t)=K_H P_g(t)$

$c(\infty, t)=c_0$

where c is the concentration of the dissolved gas in melt pitch, D is the diffusion coefficient, R is the radius of the bubble, r is the radial distance from the bubble center, $\Re$ is the ideal gas constant, P_g is the gas pressure inside the bubble, P_L is the pressure of the melt pitch, and σ is the surface tension of the melt pitch.

After the bubbles touch and collapse, the equations above have to be modified. As the spherical shape assumption is still used, R still is the radius of the assumed sphere, and the bubble volume will be the segment of the assumed sphere. The gas diffusion area will be the segment area.

The mold-filling process of the carbon foam may be considered as an isothermal process because the process takes a very short time. The mass conservation equation is as follows:

$$\frac{\partial \rho_{cell}}{\partial t} + \nabla \cdot (\rho_{cell} V) = 0$$

where ρ_{cell} is the density of a cell that consists of the bubble and the melt pitch surrounding it. If the mold thickness is smaller than its length and width, the Hagen-Poiseuille (H-P) equation can be used. Combining the mass balance and H-P equation, a Poisson equation can be obtained.

A finite element code is being developed. Two element formats were selected: tetrahedral and isoparametric. The tetrahedral element is used to connect the analysis to the mechanical property of the foam. The isoparametric element will be used in the future. The subroutines to calculate the coefficient matrix have been finished.

3.3   CONCLUSIONS

The model used in simulating the polymer foam process is modified to handle the open-cell case in the carbon form process. Nucleation, bubble growth and mold-cavity-filling will be included in the model. At this stage the spheretic bubble assumption is used. Several subroutines to calculate the coefficient matrix of FEA have been completed.

REFERENCES

1.   Roy, A. K. (1998). Three-Dimensional Mixed Variational Micromechanics Model for Textile Composites. *Proceedings of the AIAA SDM Conference*.

2.   Reissner, E. (1950). On a Variational Theorem in Elasticity. *Journal of Mathematics and Physics* (90-95).

3.   Pagano, N. J. (1978). Stress Fields in Composite Laminates. *International Journal of Solids and Structures 14* (385-400).

4.   Harrison, P. E., & E. R. Johnson. (1996). A Mixed Variational Formulation for Interlaminar Stresses in Thickness-Tapered Composite Laminates. *International Journal of Solids and Structures 33*(16) (2377-2399).

5.   Zienkiewicz, O. C., & R. L. Taylor. (1988). *The Finite Element Method*, 4th edition, Vol. 1, McGraw-Hill International Editions.

6.   Tsai, S. W. (1988). *Composite Design*, 4th edition, Think Composites, Dayton, Ohio.

7.   Zhang, Y. C., & J. Harding. (1990). A Numerical Micromechanics Analysis of the Mechanical Properties of a Plain Weave Composite. *Computers and Structures 36*(5) (839-844).

8.   Ishikawa, T., M. Matsushima, Y. Hayashi, & T.-W. Chou. (1985). Experimental Confirmation of the Theory of Elastic Moduli of Fabric Composites. *Journal of Composite Materials 19* (443-458).

9.   Naik, N. K., & V. K. Ganesh. (1992). Prediction of On-Axes Elastic Properties of Plain Weave Fabric Composites. *Composites Science and Technology 45* (135-152).

10.   Roy, A. K. (1996). *In Situ* Damage Observation and Failure in Model Laminates Containing Planar Yarn Crimping of Woven Composites. *Mechanics of Composite Materials and Structures 3* (101-117).

11.   Kim, R. Y., F. Abrams, & M. Knight. (1988). Mechanical Characterization of a Thick Composite Laminate. *Proceedings of the American Society for Composites*, *3rd Technical Conference* (25-29).

12.   Klett, J., & B. Conway. (2000). Thermal Management Solutions Utilizing High Thermal Conductivity Graphite Foams. *Proceedings of the 45th Int. SAMPE Symposium* (1933-1943).

13. Rogers, D. K., J. Plucinski, P. G. Stansberry, A. H. Stiller, & J. W. Zondlo. (2000). Low-Cost Carbon Foams for Thermal Protection and Reinforcement Applications. *Proceedings of the 45th Int. SAMPE Symposium* (293-305).

14. Warren, W. E., & A. M. Kraynik. (1988). The Linear Elastic Properties of Open-Cell Foams. *Journal of Applied Mechanics 55* (341-346).

15. Bikerman, J. J. (1973). *Foams.* Springer-Verlag, New York. (pp. 33-64).

16. Roy, A. K., D. Pullman, & K. M. Kearns. (1998). Experimental Methods for Measuring Tensile and Shear Stiffness and Strength of Graphitic Foam. *Proceedings of the 43rd Int. SAMPE Symposium.*

17. Amon, Moris, & Costel D. Denson. (1986). A Study of the Dynamics of Foam Growth: Simplified Analysis and Experimental Results for Bulk Density in Structural Foam Molding. *Poly. Eng. & Sci. 26*(3) (255-267).

18. Amon, Moris, & Costel D. Denson. (1984). A Study of the Dynamics of Foam Growth: Analysis of the Growth of Closely Spaced Spherical Bubbles. *Poly. Eng. & Sci. 24*(13) (1026-1034).

19. Arefmanesh, A., & S. G. Advani. (1992). Non-isothermal Bubble Growth in Polymeric Foams. *Cellular Polymers* (ASME, MD-Vol. 38) (25-40).

20. Arefmanesh, A., S. G. Advani, & E. E. Michaelides. (1990). A Numerical Study of Bubble Growth During Low Pressure Structural Foam Molding Process. *Poly. Eng. & Sci. 30*(20) (1330-1338).

21. Clift, Roland, J. R. Grace, & M. E. Weber. (1978). *Bubble, Drops, and Particles.* Academic Press, Inc., New York, NY.

22. Patel, Rutton D. (1980). Bubble Growth in a Viscous Newtonian Liquid. *Chemical Eng. Science 35* (2356-2358).

23. Anderson, David P., Philip G. Wapner, & David B. Curliss. (1992). Physical Property Characteristics of Pitch Materials. *Mat. Res. Soc. Symp. Proc. 270* (59-64).

24. Colton, Jonathan S., & Nam P. Suh. (1987). Nucleation of Microcellular Foam: Theory and Practice. *Poly. Eng. & Sci. 2*(7) (500-503).

25. Ramesh, N. S., Don H. Rasmussen, & G. A. Campbell. (1994). The Heterogeneous Nucleation of Microcellular Foams Assisted by the Survival of Microvoids in Polymers Containing Low Glass Transition Particles, Part II: Experimental Results and Discussion. *Poly. Eng. & Sci. 34*(22) (1698-1706).

26. Shafi, M. A., K. Joshi, & R. W. Flumerfelt. (1997). Bubble Size Distributions in Freely Expanded Polymer Foams. *Chem. Eng. Sci. 52*(4) (635-644).

27. Shafi, M. A., & R. W. Flumerfelt. (1997). Initial Bubble in Polymer Foam Processes. *Chem. Eng. Sci. 52*(4) (627-633).

28. Street, James R., Arthur L. Fricke, & L. Philip Reiss. (1971). Dynamics of Phase Growth in Viscous, Non-Newtonian Liquids. *Ind. Eng. Chem. Fundam. 10*(1) (54-64).

29. Wang, S. F., & A. A. Ogale. (1990). Structural Foam Molding: Modeling of Bubble-Growth Process Resulting from Chemical Blowing Agents. *Polym.-Plast. Technol. Eng. 29*(4) (355-369).

LIST OF ACRONYMS

Acronym	Description
EAM	element array model
FEA	finite element analysis
FPF	first-ply-failure
H-P	Hagen-Poiseuille
LBC	ligament boundary conditions
LPF	last-ply-failure
MKM	modified Kabelka's model
MMPM	modified mosaic parallel model
OBC	overall loading/boundary conditions
RVE	representative volume element
SAM	slice array model
SEM	scanning electron microscope